# JGR Solid Earth

**Key Points:**
- The amplitude spectrum of laboratory failure can resemble that of natural earthquakes
- In the laboratory, high frequency energy release may be obscured at high stress levels
- Unsteady fault slip and earthquake-like spectra are encouraged by near-critical energy release

# Near-Fault Velocity Spectra From Laboratory Failures and Their Relation to Natural Ground Motion

N. M. Beeler[1] , Gregory C. McLaskey[2] , David Lockner[3] , and Brian Kilgore[3]

[1]U.S. Geological Survey, Cascades Observatory, Vancouver, Washington, USA, [2]School of Civil and Environmental Engineering, Cornell University, Ithaca, New York, USA, [3]U.S. Geological Survey, Earthquake Science Center, Menlo Park, California, USA

**Abstract** We compared near-fault velocity spectra recorded during laboratory experiments to that of natural earthquakes. We fractured crystalline rock samples at room temperature and intermediate confining pressure (50 MPa). Subsequent slip events were generated on the fracture surfaces under higher confinement (300 MPa). Velocity spectra from rock fracture resemble the inverse frequency ($1/f$) decay of natural earthquake velocity. This spectrum can be attributed to fault creation via seismic fracturing over a wide range of spatial scales. In contrast, subsequent slips on the rough fracture surfaces are depleted in high frequency energy and falloff approximately as $1/f^2$. The $1/f^2$ spectrum is more consistent with a slider-block model obeying static-kinetic friction than a natural earthquake. The depleted high frequency content precludes the rough fault experiments from being directly analogous to natural sources. The suppression of high frequencies may have resulted from two possible factors: (1) the presence of a well-developed shear zone and coseismic damping of the fault motion by dissipation within it or, in our favored interpretation, (2) a smaller amount of energy dissipated by shearing relative to the total energy release at elevated confining pressure. In context of the latter explanation, a unifying concept that applies to these experiments, earthquakes, ground motion, and models of complex radiated motion is that high frequency radiated energy is relatively enhanced when total energy release is nearly balanced within the source region by dissipative processes. This near-critical energy release condition can be accessed at low normal stress in laboratory experiments.

## 1. Introduction

As recorded at or near the Earth's surface, the ground motion associated with waves radiated from earthquakes has characteristic spectra—for example, at high frequency, the amplitude of the displacement spectrum of a $p$- or $s$-wave depends approximately on frequency, $f$, as $1/f^2$ (e.g., Hanks & Wyss, 1972), whereas the velocity spectrum decays as $1/f$ (e.g., Brune, 1970), and, between the corner and maximum observable frequencies, accelerations are independent of frequency (e.g., Hanks & McGuire, 1981; Housner, 1947). Body waves are typically observed far from the source, and it is not known with certainty whether the characteristic spectra are due to the source or to interaction with material heterogeneities along the path from source to station. As a practical matter, the lack of dependence of ground acceleration on frequency and its random phase allows earthquake engineers to treat far-field accelerations as uncorrelated white noise at all resolved frequencies above the corner frequency, $f_c$ (Hanks & McGuire, 1981; Housner, 1947). Practicality notwithstanding, most often in studies of earthquake physics, the characteristic high frequency component of the spectrum is attributed to the source and to source "complexity." To produce a random distribution of accelerations on a discrete fault surface is thought to require slip to be spatially and temporally variable within the source, typically presumed to result from heterogeneity of some kind (Andrews, 1981). Examples are variable fault strength or variable initial stress if the fault is smooth (Andrews & Ma, 2016) or roughness of the surface of a fault with homogeneous strength (Dunham et al., 2011). Indeed, sophisticated numerical simulations of elastodynamic slip on rough, mated, rock surfaces (Dunham et al., 2011) or on flat faults with initially heterogeneous stress or fault strength (Andrews & Ma, 2016) produce ground acceleration spectra that are frequency independent. Inferences of complex motion also arise from kinematic inversions of seismograms; these produce highly heterogeneous slip distributions thought also to relate to spatially variable fault properties (e.g., Lavallee et al., 2006).

Well-instrumented laboratory experiments may constrain source contributions to the frequency content of ground motion, especially in instances where the surface and rheological properties of the fault and the physical processes in the source are well characterized. More generally, it is possible that different in-source processes (fracture, shear melting, dehydration, thermal pressurization; e.g., Ma et al., 2003) have source spectra with diagnostic properties, at least as measured near or on the fault as may be done in experiments. It is also possible that slip on rough faults has different spectra than on flat faults. Additional advantages to studying earthquake faulting in experiments are that, in principle, the stresses and fault strength are measured directly and relatable to slip, slip velocity, and acceleration. Nonetheless, to our knowledge, the triaxial experiments reported in this study are the first in which high rate recordings of near-source velocity have been made at sufficient resolution during faulting at natural rates (>0.5 m/s). Previously, McLaskey, Kilgore, et al. (2015) reported time series of single point on-fault velocity measurements during two large complex ruptures at low normal stress and somewhat lower slip rates.

In this study, following McLaskey et al. (2012) and McLaskey and Lockner (2014), who used displacement spectra from piezoelectric sensors, the characteristics of near-fault velocity spectra are compared with that of natural body waves. Because it is widely assumed that the complexity of natural ground motion derives from the source, the focus is on two experimental end-member cases intended to produce complex motion. The first case is dynamic rock fracture: experiments conducted on initially intact cores of Westerly granite and Devil's postpile basalt with 25.4-mm diameter. Rock failure involves fracture over the full range of possible scales, from grain boundaries to the whole sample (Moore & Lockner, 1995). Consequently, the failure processes are expected to be complex, representing the fracture end-member, as may be observed in some mining-induced earthquakes. The tests are conducted dry at intermediate confining pressure $\sigma_c$ (50 MPa), and the fault normal stresses at failure are 187 and 194 MPa. The corresponding stress conditions in the Earth's crust can be estimated from the increase of overburden with depth, $\rho g h$, where $\rho$ is density, $g$ is acceleration due to gravity, and $h$ is depth. An estimate of the effective overburden in the saturated crust is the dry overburden gradient ($\rho = 2800$ kg/m$^3$), 28 MPa/km, minus that due to hydrostatic pore pressure ($\rho = 1000$ kg/m$^3$), 10 MPa/km, or 18 MPa/km (Tse & Rice, 1986). Assuming that fault effective normal stress is approximately equal to overburden, the stress in these experiments corresponds to crustal levels near the base of the seismogenic zone at approximately 10 km. These rock failures produce velocity spectra that are largely consistent with natural earthquakes.

However, rather than rock failure, more often earthquakes are thought to occur on preexisting faults. Recent theoretical physical models of earthquake source complexity (e.g., Dunham et al., 2011; Andrews & Ma, 2016), which assume a preexisting fault zone, require geometrical or heterogeneous properties to produce complex source motions that are consistent with earthquakes. To address the role of preexisting heterogeneity, taking an approach similar to Goebel et al. (2014), the second set of experiments is failure tests on the geometrically complex fault surfaces and nascent shear zones generated in the intact failure experiments. The rock failures produce rough surfaces, fractures, rock debris, and gouge, all of which tend to increase the fracture energy and rate dependence of subsequent slip events above that of the typical flat smooth surfaces used in more conventional stick-slip studies (e.g., Passelègue et al., 2016; Kilgore et al., 2017). To assure subsequent seismic events, the confining pressure was raised by a factor of 6 to 300 MPa. Using the same extrapolation to depth approach detailed above, normal stress at failure in these tests corresponds to 490 to 500 MPa, appropriate for depths of 27 to 27.5 km. While the experimental choice to increase confining pressures is successful in producing recurring slip events on very rough fault surfaces, the resulting spectra are depleted at high frequency and not consistent with natural earthquakes. Ultimately, we will attribute the suppression of high frequency radiation as an experimental artifact of the excessive stress level that arises independent of the actual geometric complexity of the source.

## 2. Experiments

The experiments were conducted at room temperature and humidity in a triaxial geometry (Brace, 1964). Like Goebel et al. (2014), the sequences are rock failures followed by slip events on the fractured surfaces. There are two rock failure events, one on Westerly granite and the other on Devil's postpile basalt at 50 MPa confining pressure. There are four (two following each failure of an initially intact rock sample) subsequent
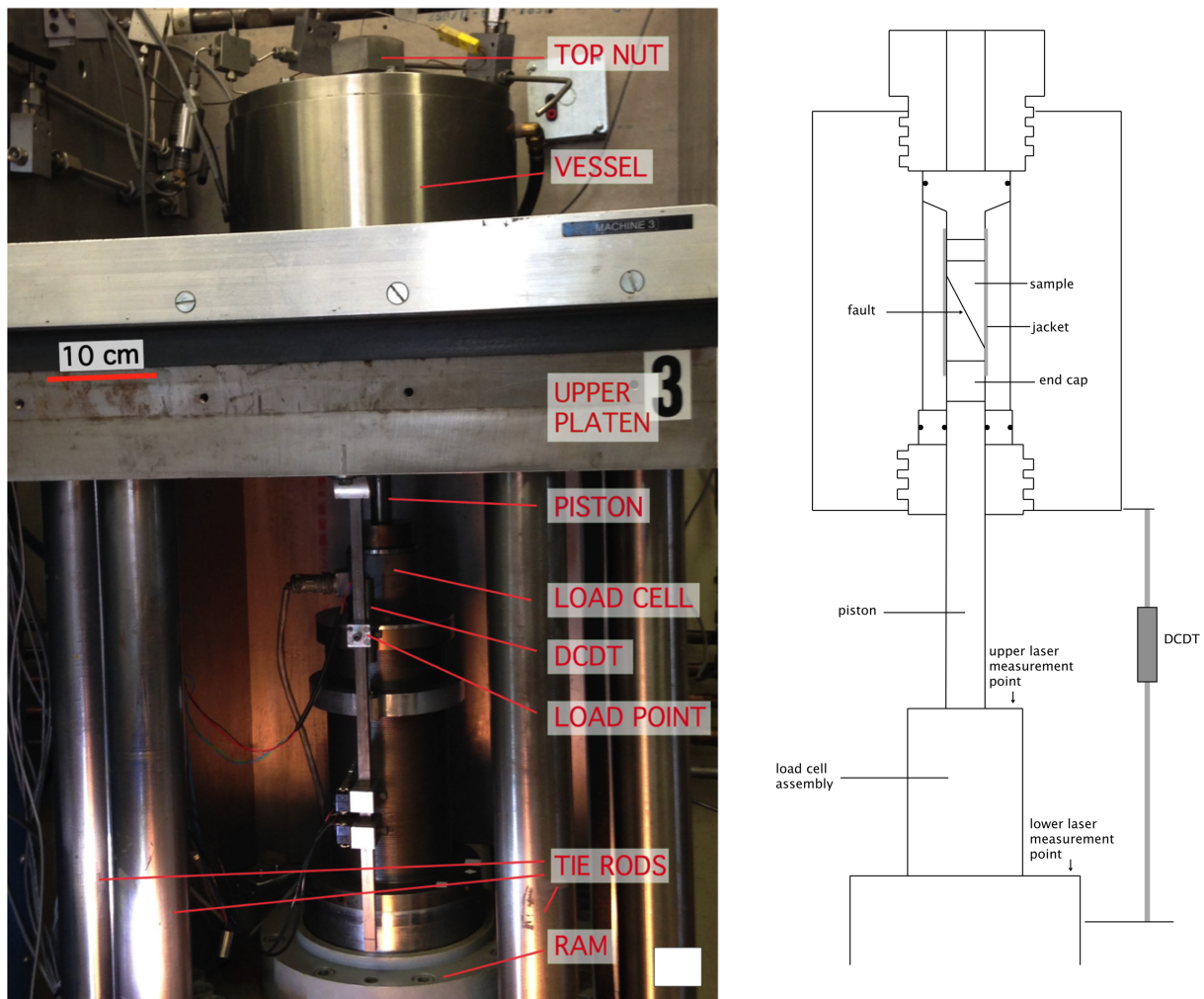
**Figure 1.** Triaxial experimental configuration. Left: labeled photograph. Samples are placed in the pressure vessel (top) and axial force is applied by a hydraulic ram (bottom). Right: schematic diagram of the sample within the vessel. Axial load (load cell), displacement transducer (DCDT), and velocity (arrows) are measured outside the pressure vessel.

slip events on fractured surfaces at 300 MPa. The experiments are from a wide-ranging suite of tests, first reported by Lockner et al. (2010). In contrast to the rock failure and rough fault reported here, a companion study (Lockner et al., 2017) details stick-slip on smooth (#600 grit) saw cut faults from the Lockner et al. (2010) experiments. Conventional triaxial compression used in all these studies is an axisymmetric configuration in which a jacketed cylindrical sample is placed in a chamber that is pressurized with a fluid (Figure 1). Then, deviatoric stress is applied by advancing a piston against the sample end. Room-dry cylindrical samples of granite and basalt with 25.4-mm diameter and 63.5-mm length were tested at constant confining pressures. Samples were placed between steel end caps and slipped into a polyurethane tube with 3.2-mm wall thickness to isolate them from the confining fluid, here silicone oil. The piston was advanced under computer control using a proportional servo-control system. A 0.12-mm-thick greased Teflon shim was placed between the piston and the steel end cap to allow lateral slip of the lower sample half that accommodates shearing on the inclined fault. Confining pressure, axial load, and piston displacement were recorded continuously at 1 Hz. A displacement transducer (DCDT) is used for controlling the position of the loading piston. The DCDT is also recorded by a continuous 100-Hz system to resolve piston motion immediately following a slip event. Additional details of the experimental measurements and procedures are found in Lockner et al. (2017).

The rapid and transient stick-slip motion of the axial piston in these tests was measured outside the pressure vessel with two single-point laser Doppler vibrometers (LDV) (Figure 1b). An advantage of the LDV is that, unlike other high frequency sensors (piezo-displacement transducers or accelerometers), they are noncontact sensors that lack internal moving parts, instrument response corrections, and resonances (c.f., Schubnel et al., 2011; McLaskey, Lockner, et al., 2015). Each instrument is mounted on a tripod that stands on the concrete floor of the laboratory. The floor provides a stable and stationary reference for the LDV velocity measurements, and the instruments are well isolated from any vibrations of the floor induced by the slip events. Velocities were recorded on two separate data acquisition systems. The primary velocity measurements use a Polytec model OFV-5000 vibrometer controller and an OFV-505 vibrometer sensor head. The controller has a velocity decoder response from DC to 2.5 MHz. This instrument is referred to as the upper laser throughout this report. The upper laser is directed at the top surface of the load cell assembly (perpendicular to the piston axis) immediately below the bottom of the piston and above the top surface of the hydraulic ram (Figures 1a and 1b). The target surface is 26 cm below the center of the fault. The LDV is directed at the surface by means of a mirror held by an extending arm attached to a separate, free-standing cart. The upper vibrometer has a maximum frequency of 250 KHz and is low pass filtered at 100 KHz for direct comparison with the output of the lower laser (see below). The velocity output from the upper laser is recorded for 1 s about the trigger using a pretrigger/posttrigger transient waveform recorder, saving data to disk at the rate of a million samples per second. The lower LDV consisted of an OFV-2600 vibrometer controller and an OFV-352 vibrometer sensor head. It has a maximum response rate of 100 kHz. The lower laser records the velocity of the top surface of the ram immediately below the load cell assembly (Figures 1a and 1b). This measurement is 37.1 cm below the center of the fault. The velocity of the lower laser is the trigger of the 1 MHz recording system and is recorded on that system.

## 2.1. Velocity Time Series and Their Spectra

To compare measurements of source properties of laboratory-scale earthquakes to their natural counterparts, ideally the measurements would be made in similar proximity to the source. Unfortunately most natural spectra from body waves are made in the far-field, and our measurements are in the near-field. The far-field is the portion of the wave field where the propagating dynamic stresses or displacements are large relative to their static equivalents, and the static contributions can be neglected. So, for example, in the far-field the displacement associated with an s-wave has no resolved net offset and integrates to a constant that depends on the duration, the net source offset, and the source to measurement distance. Static displacements decay with distance more rapidly than the amplitude of dynamic waves. For example, in an axisymmetric geometry, static displacements decay at a maximum reduction of $1/r^2$, where $r$ is radial distance from the source (Cotton & Coutant, 1997), while the dynamic displacement goes as $1/r$. Accordingly, a practical definition of the far-field is beyond a few fault lengths from the source. As previously discussed in section 1, the standard assumption made about source physics in seismology is that the frequency content measured from far-field body waves is representative of the source itself, despite the large separation.

The near-field is that which contains essentially all of the elastic strain energy released by the earthquake that is stored in the immediate surroundings. In a laboratory setting, source measurements would ideally be made in the extreme near-field, across the fault itself as in a stick-slip lab test (e.g., Kilgore et al., 2017), measuring the static offset, duration and fault slip velocity directly. The velocity measurements in this study are made off the fault, outside the pressure vessel on the piston (Figure 1), but still in the near-field. In laboratory faulting, the testing machine provides a significant amount of the stored elastic energy that is released during the sample scale-slip events, and the machine always experiences a net decrease in elastic strain in response to a stress drop. Thus, by definition and regardless of the size of the fault, measurements made in a laboratory test during a system-scale failure (sample-scale) are in the near-field and contain at least some component of static change. The standard seismological assumption is also used here: The frequency content measured from the on-piston near-field measures is representative of the source itself. There is additional discussion of this assumption in section 2.2.

The standard seismological analysis for frequency content of the source is to calculate the amplitude spectra, $A(\omega)$, from the Fourier transform of the time series:

$$A(\omega) = \sqrt{R(\omega)^2 + I(\omega)^2},$$
(1)

where $\omega = 2\pi f$ is the angular frequency, $f$ is frequency, $R(\omega)$ is the real, and $I(\omega)$ is the imaginary part of the complex frequency series that results from the transform. Primarily, spectra used in this report are calculated from the upper laser time series (Figure 2). It is important to establish that our choice of record duration did not influence the shape of the spectra. Figure 2 shows the same slip event for four different time scales/windows of 0.2, 0.02, 0.002, and 0.00035 s, respectively. In the following discussion, these are referred to as the long, intermediate, short, and shortest records. Each of these windows has one fourth of the respective window length prior to the event onset and three fourths following. The first three windows, parts (a–c), of Figure 2 are at scales decreasing by a factor of 10. The longest time series of 0.2 s duration (Figure 2a) effectively shows the entire record of significant velocity excursions. The peak velocity is very close in time to the trigger of the recording system at approximately $t = 0.25$ s. Immediately following the onset, a brief period of high frequency oscillation occurs (Figures 2b and 2c), followed by a ringing that decays down toward background. This ringing defines the long period resonance of the testing machine, a period of about 0.002 s, that is initiated by the rapid slip event. This is the resonance of the test machine frame, consisting of four steel posts, two steel platens, and the pressure vessel. In the intermediate time series (Figure 2b), the long period resonance is more clearly resolved, and a second, shorter immediate oscillation is visible. This second oscillation corresponds to the resonance of the axial piston that directly loads the sample. This is the most compliant element in the loading system (Shimamoto et al., 1980) and is equivalent to the time constant, $T/2$, that influences the on-fault event duration in slider-block representations of fault and test machine interactions during stick-slip (Johnson & Scholz, 1976, Shimamoto et al., 1980; see Appendix A and section 2.2). In the shortest window (Figure 2d), the record length is limited to the initial positive velocities of the time series; it is truncated at the first zero crossing of velocity.

Velocity amplitude spectra of the windows (Figure 2) are shown in Figure 3. In the longest (Figure 2a and Figure 3a), the long period ringing of the apparatus is manifest as a peak in the spectra at ~500 Hz. Other than this resonance, there is little difference between the spectral shape or DC amplitude of the long (Figure 3a), intermediate (Figure 3b), and short (Figure 3c) time windows. To emphasize the similarity in shape and amplitude, the same reference spectrum (red) is shown in all three parts. The reference is calculated with the generic relationship:

$$A(f) = \frac{a_0}{\left(f_c^2 + (2\pi f)^2\right)^n}$$
(2)

where $a_0$ is a constant with dimensions of displacement/time$^{2n}$. For the reference shown, $n = 1$, $f_c = 45$ kHz, and $a_0$ is an acceleration amplitude, $a_0 = 2.5 \times 10^5$ m/s$^2$.

Figure 3d departs from the window choices in Figures 3a–3c; nonetheless, the shape is the same, and the amplitude and corner frequency are shifted slightly. A representative reference (blue) calculated from (2) with $n = 1$, $f_c = 20$ kHz, and $a_0 = 7 \times 10^4$ m/s$^2$ indicates a characteristic frequency that differs only by a factor of 2 and a DC amplitude, $a_0/f_c^2$, that differs by 33% to 50% from the long duration windows. The differences between the corner frequency and DC amplitudes of the long, intermediate, and short time windows (higher frequency) and the shortest window (lower frequency) may be due to contributions from fault zone fracture energy lengthening the event duration (e.g., Beeler et al., 2012). For more direct comparison, Figure 3e collects all of the spectra, shown with reference slopes of $1/f$ and $1/f^2$. The ensemble comparison between the spectra of a single event (Figure 3) is typical of similar comparisons made for other events in this study and demonstrates that spectral shape does not depend strongly on choice of window length.

### 2.2. Slip Duration

Despite the spectra not depending strongly on choice of time series duration, a duration choice has to be made for intra-event and event-to-reference comparisons. A goal of this study is to determine properties of the source itself, isolating its contributions. Most ideally the measurements would be made across the fault, rather than involving near-fault path effects such as reflection, scattering, and attenuation. To minimize path effects and to adhere as closely to seismic source models of on-fault motion, the shortest possible
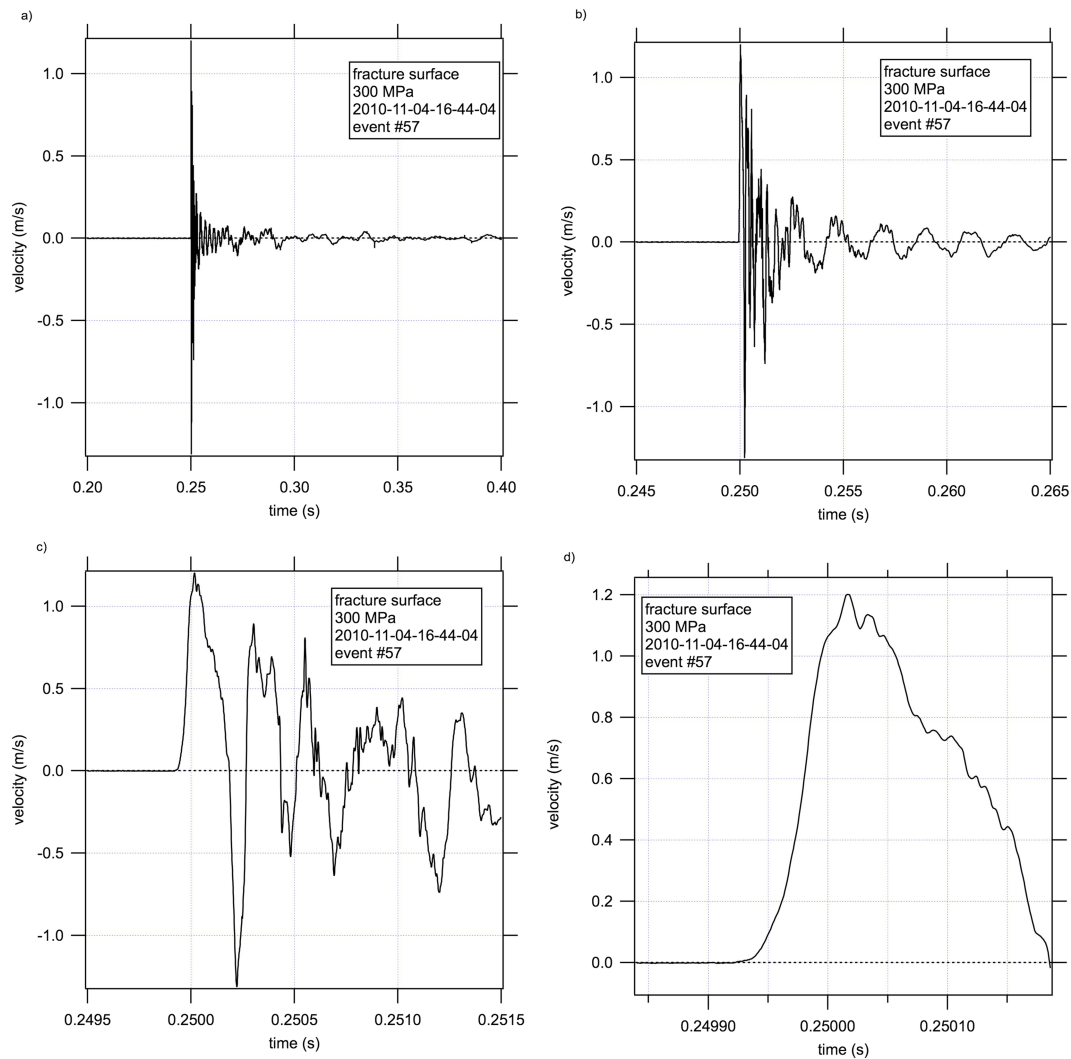
**Figure 2.** Example upper laser vibrometer record at four different time scales. Piston velocity during rapid slip on a rough shear fracture fault surface at 300 MPa confining pressure. The laser measures the piston velocity immediately above the load cell. (a) Time series of 0.2-s duration showing ringing down of the apparatus following the event. The prominent oscillation is the long period resonance of the testing machine with period of about 0.002 s. (b) Time series of 0.02-s duration showing the long period machine resonance of part (a) and a shorter period oscillation corresponding to the resonance of the axial piston. (c) Time series of 0.002-s duration. (d) Time series of 0.00035-s duration that extends only over the initial positive velocities of the time series.

duration choice was used. This is the case shown in Figure 2d, where the initially positive piston velocities define a duration $\Delta t$. This definition is the same as used in the original study (Lockner et al., 2017). Validity of comparisons with natural earthquakes entails implicit assumptions that (I) all of the frequency content within this initial period of positive velocity derives from source, (II) that $\Delta t$ is long enough to sufficiently capture the essential content of the source, and (III) that there is no frequency-dependent attenuation between the source and measurement points. Assumptions (I) and (II) are strongly supported by the spectra shown in Figure 3. Assumption (III) is expected from the apparatus design requirement that all load-bearing components are elastic. Since all events use the same duration definition, intra-event comparisons are independent of these assumptions; it is only comparisons with spectra of natural earthquakes that are affected if (I) to (III) do not hold. Subsequent studies that add across-fault slip, slip rate, or on-fault acceleration measurements can fully verify (I) to (III).

In the remainder of this report, spectra are calculated using records that start at a time $3\Delta t$ prior to the event start and end at the first zero crossing. The records are four times longer than the event itself and allow the corner frequency to be resolved. The noise level in the records was determined by taking the spectra that
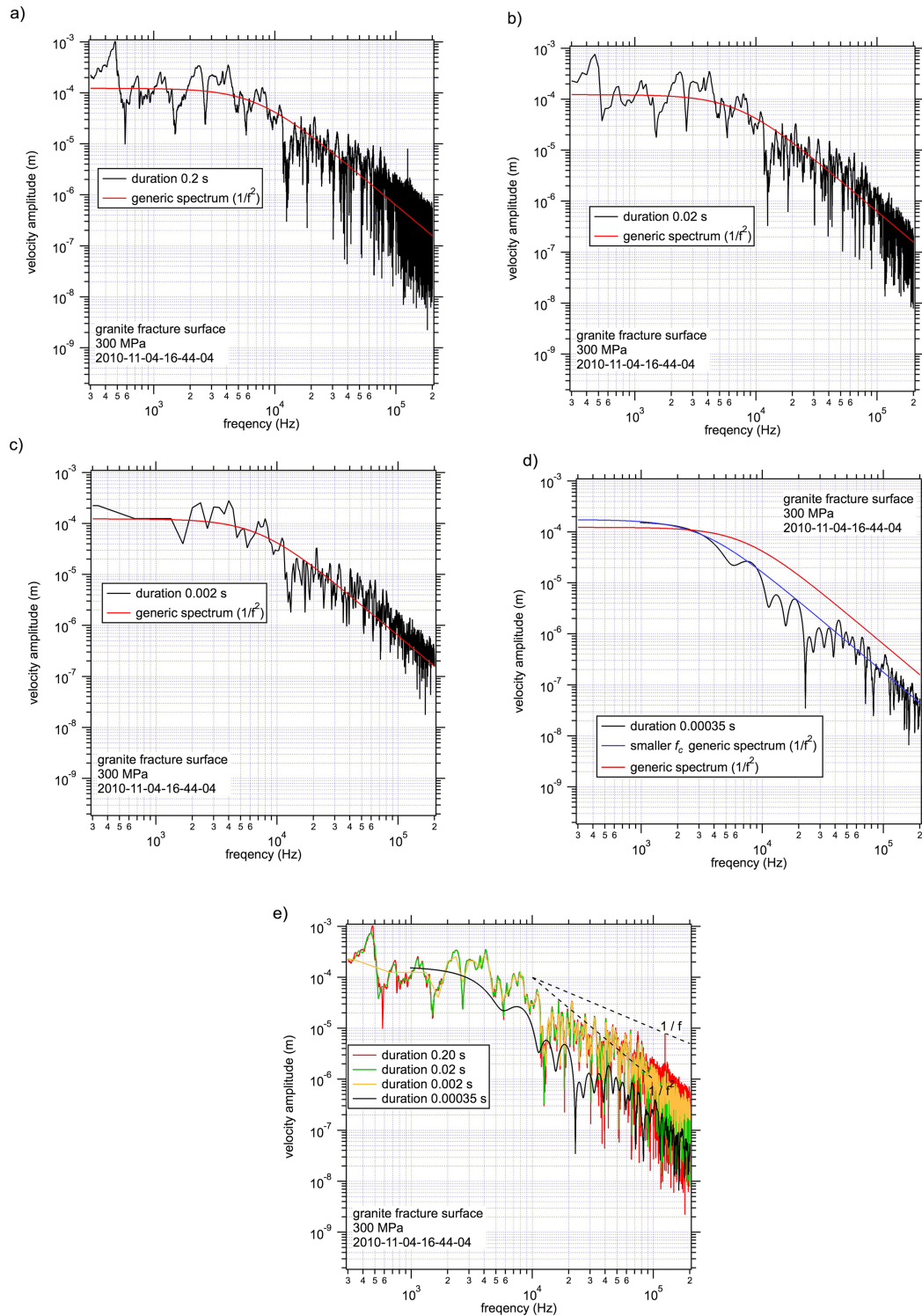
**Figure 3.** Velocity amplitude spectra determined for the event shown in Figure 2. (a) 0.2-s duration. The ringing down of the apparatus seen in the time series is manifest as a peak in the spectra at ~500 Hz. (b) 0.02-s duration. (c) 0.002-s duration. There is little difference in the spectra of parts (a–c). The long period resonance is not visible at the time scale of part (c). To emphasize the similarity in shape and amplitude of the spectra in parts (a–c), the same reference spectrum (red) is shown in all three parts. (d) The spectrum for 0.00035-s duration that extends only over the initial positive velocities of the time series. A reference representation of the spectrum (blue) is shown for comparison with that from parts (a–c) (red). (e) Collection of all the spectra from parts (a–d). Reference slopes of $1/f$ and $1/f^2$ are shown.

**Table 1**

*Source properties: From left to right in the table, reference number, sample configuration, confining pressure, static stress drop, fault slip, upper laser duration, lower laser duration, average fault slip speed, coseismic displacement upper laser, and coseismic displacement lower laser*

| # | Description | $\sigma_c$ (MPa) | $\Delta\tau_s$ (MPa) | $\Delta\delta$ (mm) | $\Delta t_{v1}$ (s) | $\Delta t_{v2}$ (s) | $\widehat{V}$ (mm/s) | $\Delta\delta_{v1}$ (mm) | $\Delta\delta_{v2}$ (mm) |
|----|----------------|------|-------|------|---------|---------|------|-------|-------|
| 55 | Intact granite | 50 | 236.0 | 2.16 | 0.00048 | 0.00048 | 4500 | 0.313 | 0.088 |
| 56 | Fractured granite | 300 | 252.8 | 1.76 | 0.00023 | 0.00024 | 7652 | 0.113 | 0.050 |
| 57 | Fractured granite | 300 | 282.0 | 1.96 | 0.00025 | 0.00022 | 7840 | 0.164 | 0.052 |
| 58 | Intact basalt | 50 | 247.7 | 2.93 | 0.00066 | 0.00069 | 4440 | 0.464 | 0.122 |
| 59 | Fractured basalt | 300 | 285.8 | 2.01 | 0.00023 | 0.00026 | 8739 | 0.155 | 0.057 |
| 60 | Fractured basalt | 300 | 290.0 | 2.03 | 0.00022 | 0.00026 | 9227 | 0.137 | 0.053 |

start $5\Delta t$ prior to the event onset and end $2\Delta t$ prior to the event. These spectra are shown with those of the event to document the noise (instrument and environment) and its frequency dependence. To summarize the intent of these choices, the noise spectra are from records with the same duration as those used to determine the event spectra and overlap with event records well prior to the event start, between $3\Delta t$ and $2\Delta t$ prior to the onset.

The physics that determines event duration in earthquakes and in experiments is not the same. The standard, first-order experimental event duration is half the piston resonance period (the return time of reflected waves to the fault, having traveled over the most compliant element in the apparatus (Shimamoto et al., 1980)). In slider-block representations with static-kinetic fault strength, this nominal duration is

$$\Delta t_n = 2\pi\sqrt{\frac{m}{Ak}}, \qquad (3)$$

where $A$ is fault area, $k$ is effective elastic stiffness of the fault and machine (see below), and $m$ is mass (*Johnson and Scholz*, 1973). For the triaxial testing machine used, $\Delta t$ for slip on smooth, flat fault surfaces is ~10 ms (Kilgore et al., 2017; Lockner et al., 2017) and can be considered an upper bound on $\Delta t_n$. Energy dissipated in dropping strength from peak to sliding strength is expected to increase the duration, $\Delta t > \Delta t_n$ (e.g., Beeler et al., 2012). This increase is observed in the measured durations between 20 and 70 ms (Table 1). Values of the corner frequency $f_c = 1/\Delta t$ are shown for reference in plots of spectra throughout this report.

In contrast, for a natural earthquake, the corner likely relates to elastic wave speed $V_s$ and the longest dimension of the fault $L$, for example, for rupture propagation of an expanding crack at near the shear wave speed, approximately as $\Delta t = 0.9 L/V$ (Kilgore et al., 2017). Equivalently, the corner frequency is $f_c = 1.1 V_s/L$. As a reminder of the different physics, for a second reference frequency, an estimated equivalent from our experiments is that associated with shear rupture propagation across the entire fault, $f_{tt} = 0.9 V_s/L$.

## 2.3. Machine Interactions and Source Properties

Spectra of laboratory failures may be influenced by interactions with the machine at shorter time scales than the event duration. In particular, in all laboratory geometries, there are high elastic contrast interfaces in close proximity to the fault; in a triaxial testing machine, these are located between the rock samples and steel loading pistons. Thus there is always a source of elastodynamic reflection of one sample dimension away from the fault. Here and throughout the rest of the paper, the reflection time is characterized by the estimated frequency of the first shear wave reflection $f_{fr} = V_s/2Z$, where $V_s$ is the shear wave speed and $Z$ is the distance between the fault and the closest interface. To summarize the relations between these characteristic frequencies, in experiments, the event duration is longer than the return time of reflections to the fault surface and longer than the travel time of rupture across the whole fault, $f_c < f_{fr}$ and $f_c < f_{tt}$, while for a natural fault, $f_c < f_{fr}$ and $f_c \approx f_{tt}$.

As detailed in Lockner et al. (2017), seismic laboratory failures in this apparatus occur much more rapidly than the servo-controlled axial loading can accommodate. As a result, there are three relevant machine stiffnesses: the controlled loading stiffness, $k_{xl} \approx 149$ MPa/mm, that reflects the compliance between the

mounting points of the DCDT (Figure 1); a seismic unloading stiffness $k_T \approx 133$ MPa/mm of the entire system (machine, samples, fault) that relates the static stress drop of the slip events to the coseismic fault displacement; and a third stiffness $k_m \approx 1270$ MPa/mm that represents the compliance not accounted for by $k_{xl}$ ($k_m = [1/k_T - 1/k_{xl}]^{-1}$). The nominal stiffness values quoted throughout this report were compiled for Lockner et al. (2010) and are defined as changes in shear stress on a plane inclined at 30° from the piston axis due to axial displacement, $d\tau/dx$. Thus, implicit in the slip and stress drop estimates that follow is the assumption that faults generated by intact failure are oriented 30° from the sample axis. Slip, $\delta$, relates to axial displacement, $x$, as $\delta = x/\cos 30°$. Coseismic fault slip $\Delta\delta$ and static stress drop $\Delta\tau_s$ (Table 1) were estimated from the coseismic axial stress and load point displacement (DCDT) records using the known stiffnesses and the procedures described in Lockner et al. (2017).

The event durations determined from the vibrometer records when combined with fault slip define average coseismic fault slip rates $\widehat{V} = \Delta\delta/\Delta t$ (Table 1). These slip rates are quite high, ranging from 4.4 to 9.4 m/s, though perhaps not unreasonable for high stress drop natural earthquakes. The relation between average velocity and static stress drop is approximately linear as would be expected from elastodynamics [c.f., Brune, 1970]. The scaling is similar to the elastic impedance (Kilgore et al., 2017) but with a nonzero intercept (Figure 4a). In prior faulting experiments, the stress drop-velocity intercept ($\widehat{V} = 0$) has been interpreted as a constraint on failure initiation and in-source dissipation (Beeler et al., 2012). According to this argument, the stress drop intercept is that necessary to initiate failure and produce a finite coseismic slip speed. For instance, the minimum strength loss for unstable fault slip in linear slip weakening earthquake nucleation models is $\Delta\tau^{min} = k_T\, d_c$, where $d_c$ is a weakening distance. Taking the observed intercept to represent that minimum, $\Delta\tau^{min} = 179$ MPa, and using the known unloading stiffness (133 MPa/mm), the weakening distance estimate is $d_c = 1.3$ mm. This is ~50 times larger than inferences from rupture on flat ground 60 grit granite surfaces, 25 to 33 μm (Beeler et al., 2012; Okubo & Dieterich, 1984), but probably not unreasonable. The associated minimum linear weakening fracture energy estimate, $G_e^{min} = \Delta\tau^{min}d_*/2$ (after *Palmer and Rice*, 1973), is 119 kJ/m$^2$. This value exceeds those inferred from controlled quasi-static failure tests on intact crystalline rock by between 30% to an order of magnitude (Lockner et al., 1991; Moore & Lockner, 1995; Wong, 1986). While this might be interpreted to suggest that in the laboratory seismic energy release produces more fracture energy, given the approximate nature of our estimate and the differences between the experimental approaches, the difference may not be significant.

Coseismic propagating displacements from fault slip are also recorded by the vibrometers. Integrating the velocity time series from the event onset to $\Delta t$ produces net coseismic axial displacements of the instrument targets, $\Delta\delta_{v1}$ and $\Delta\delta_{v2}$ (Table 1). Both of these displacements scale linearly with fault slip (Figure 4b), thus, are slip proxies and are linear with one another (Figure 4c). The more remote lower laser measures approximately one third of the coseismic displacement of the upper laser. The upper laser displacement is roughly six times smaller than the estimated coseismic fault displacement. These differences are expected. Indeed, following Lockner et al. (2017) and using the nominal stiffnesses, coseismic motion of the load point (compliance between the mounting points of the DCDT) is expected to be more than ten times smaller than the causative fault slip. These differences between fault slip and displacements measured elsewhere in the loading column reflect the near-field decay of static elastic distortion with distance from the source.

## 3. Velocity Time Series and Spectra

### 3.1. Rock Failure

Failure of initially intact rock follows a somewhat erratic variation of velocity with time (Figure 5a). The event duration for granite failure is around 0.5 ms, resulting in a measured corner frequency, $f_c = 1818$ Hz. The duration is longer than the nominal estimate associated with slip on flat preexisting faults (Lockner et al., 2017), likely reflecting an increase in dissipation within the source during failure (e.g., Wong, 1982). This is also consistent with relatively large fracture energy estimated in the preceding section. Above the corner, the spectra fall off at a rate consistent with $1/f$ out to near 100 kHz (Figure 5b). Comparison with the spectrum from the lower laser (gray; Figure 5b) indicates that the spectral shape is independent of distance from the fault.
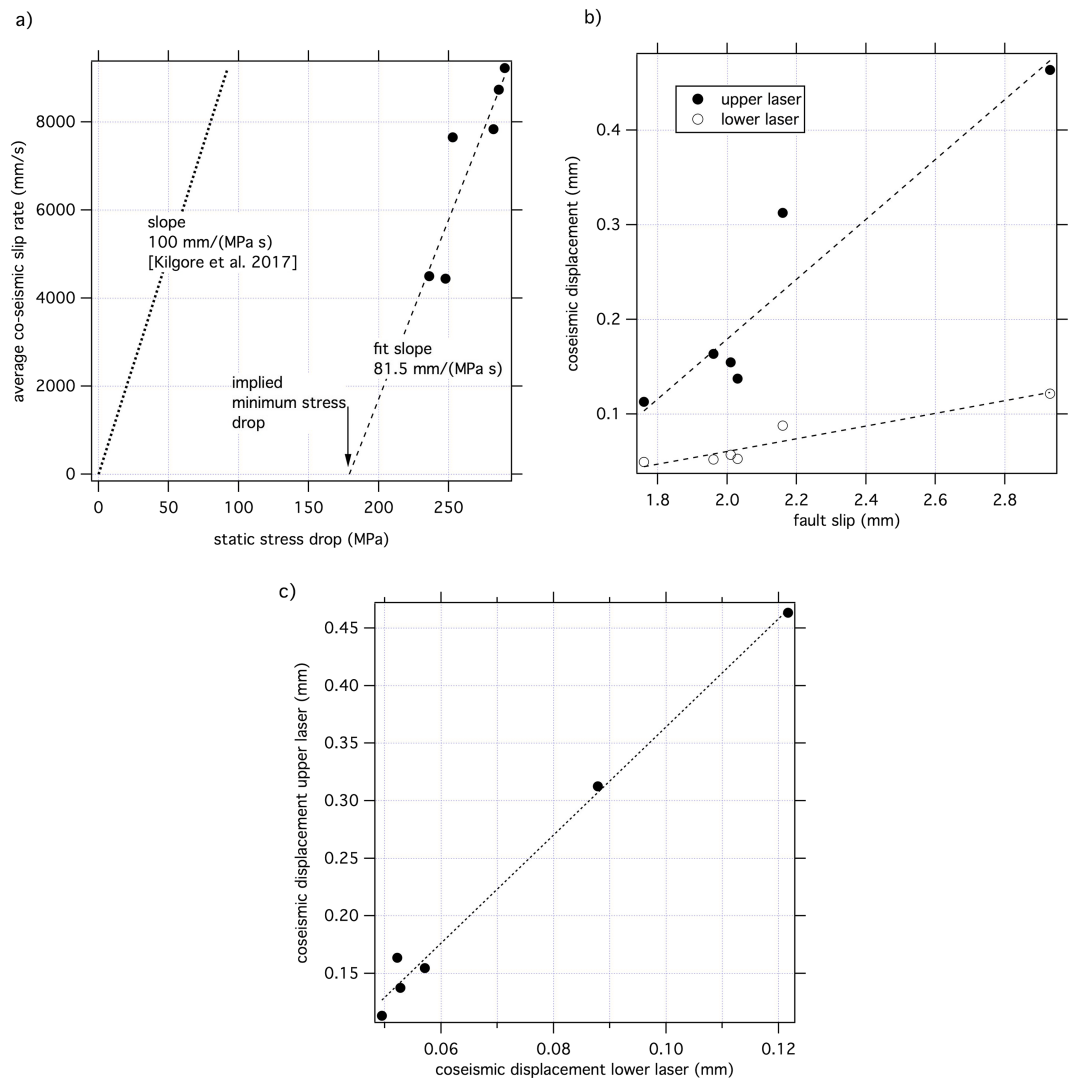
**Figure 4.** Coseismic source properties. (a) Average slip speed versus static stress drop. The reference line that passes through the origin represents the expectation from simple elastodynamic models of earthquake sources and laboratory experiments (Kilgore et al., 2017). The reference has a slope of 100 mm/(MPa s), approximately the value of the ratio of the shear wave speed to shear modulus of crystalline rock (3000 m/s/30,000 GPa). (b) Net coseismic displacement measured by the two laser vibrometers versus fault slip. (c) Scaling between net coseismic displacement measured by the two laser vibrometers.

Rupture travel and reflection times are estimated assuming a 30° angle between the fault and the axis of the loading piston and $\beta = 3543$ m/s, the elastic wave speed from Martin et al. (1990) for Westerly granite, resulting in rupture travel and reflection frequencies $f_{tt} = 6.97 \times 10^4$ Hz and $f_{fr} = 5.58 \times 10^4$ Hz. These frequencies are not associated with particular features in the time series or spectra. This should not be taken as an indication that the machine is playing a passive role during the slip event, only that there are not strong resonances at these frequencies.

Similar results are found for the basalt failure event (Figure 6a). The time series is arguably even more complex than the granite failure event. The resulting corner $f_c = 1522$ Hz is lower than for granite (Figure 6b). These features may reflect a higher fracture energy for basalt than granite, though these are single events and do not account for sample to sample variability. Shown for reference in gray (Figure 6b) is the spectrum from the lower laser, showing that the spectral shape is independent of distance from the fault. The rupture travel and reflection times are estimated assuming the same 30° angle and $\beta = 3790$ m/s from Simmons
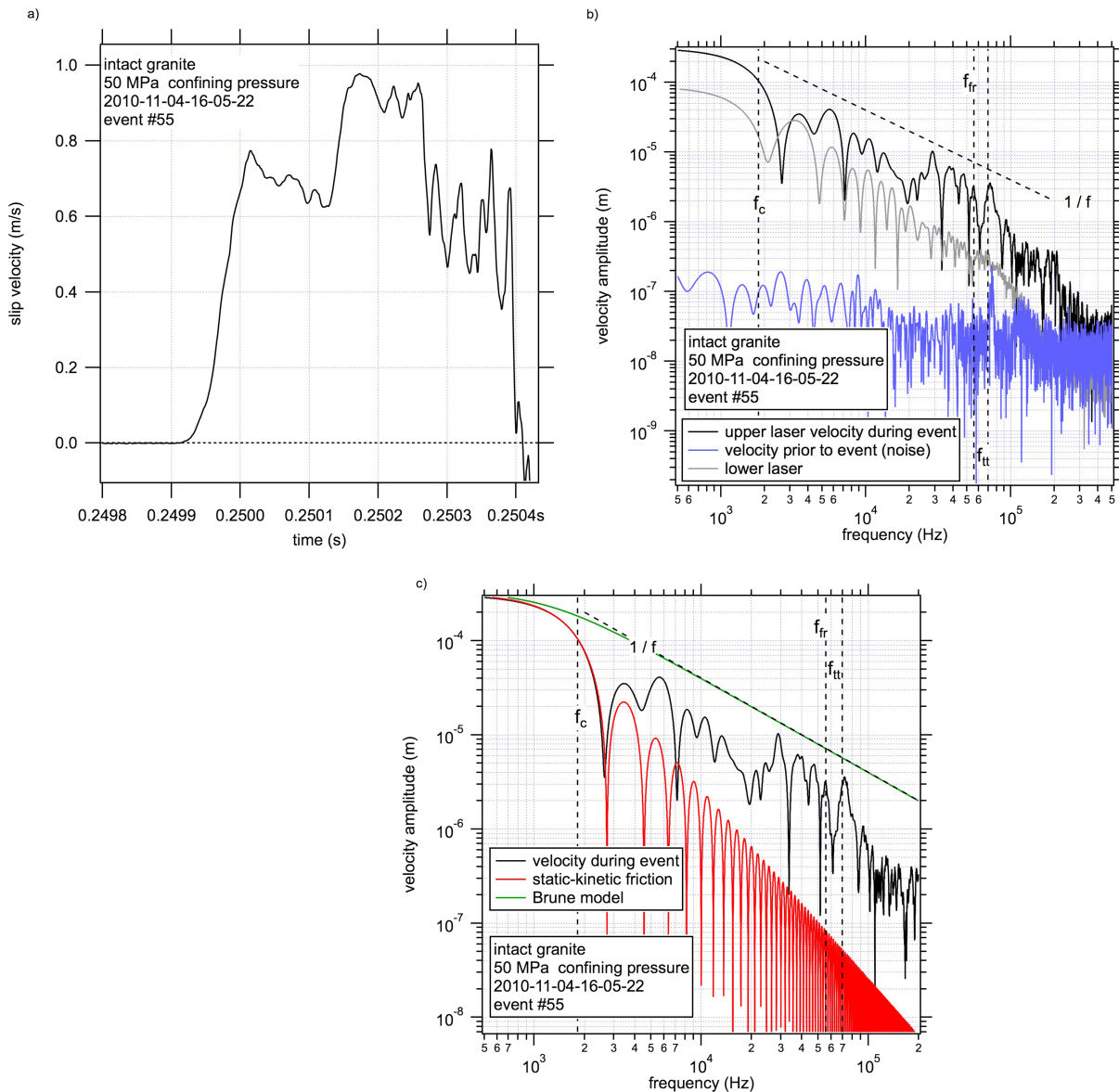
**Figure 5.** Velocity time series and amplitude spectra from failure of initially intact granite at 50 MPa confining pressure. (a) Slip velocity time series. (b) Velocity amplitude spectrum with noise level (blue), lower laser spectrum (gray), and 1/f reference. (c) Spectrum shown in part (b) with the velocity spectrum of a slider-block model following a static-kinetic fault strength (*Johnson and Scholz,* 1973) as a reference (red). A Brune model is shown for additional reference (green).

(1964), resulting $f_{tt} = 7.46 \times 10^4$ Hz and $f_{fr} = 5.97 \times 10^4$ Hz. As for granite, there are no strong resonances at these frequencies.

### 3.2. Rough Fault Surfaces

To access possible contributions of surface roughness to source spectra, tests were conducted on the extremely rough fault surfaces that were produced by a prior shear fracturing event. The rock failure process also produces fractures, rock debris, and gouge (e.g., Goebel et al., 2014; Moore & Lockner, 1995). Along with the surface roughness, each of these factors individually tends to increase the fracture energy of subsequent slip events above that of the typical flat smooth surfaces used in stick-slip studies (Lockner et al., 2017) and also is expected to make the shear zone more rate strengthening (e.g., Dieterich, 1981). Because high fracture energy and more positive rate dependence promote stable fault slip, to assure a seismic event, the confining pressure was elevated to 300 MPa in these tests.
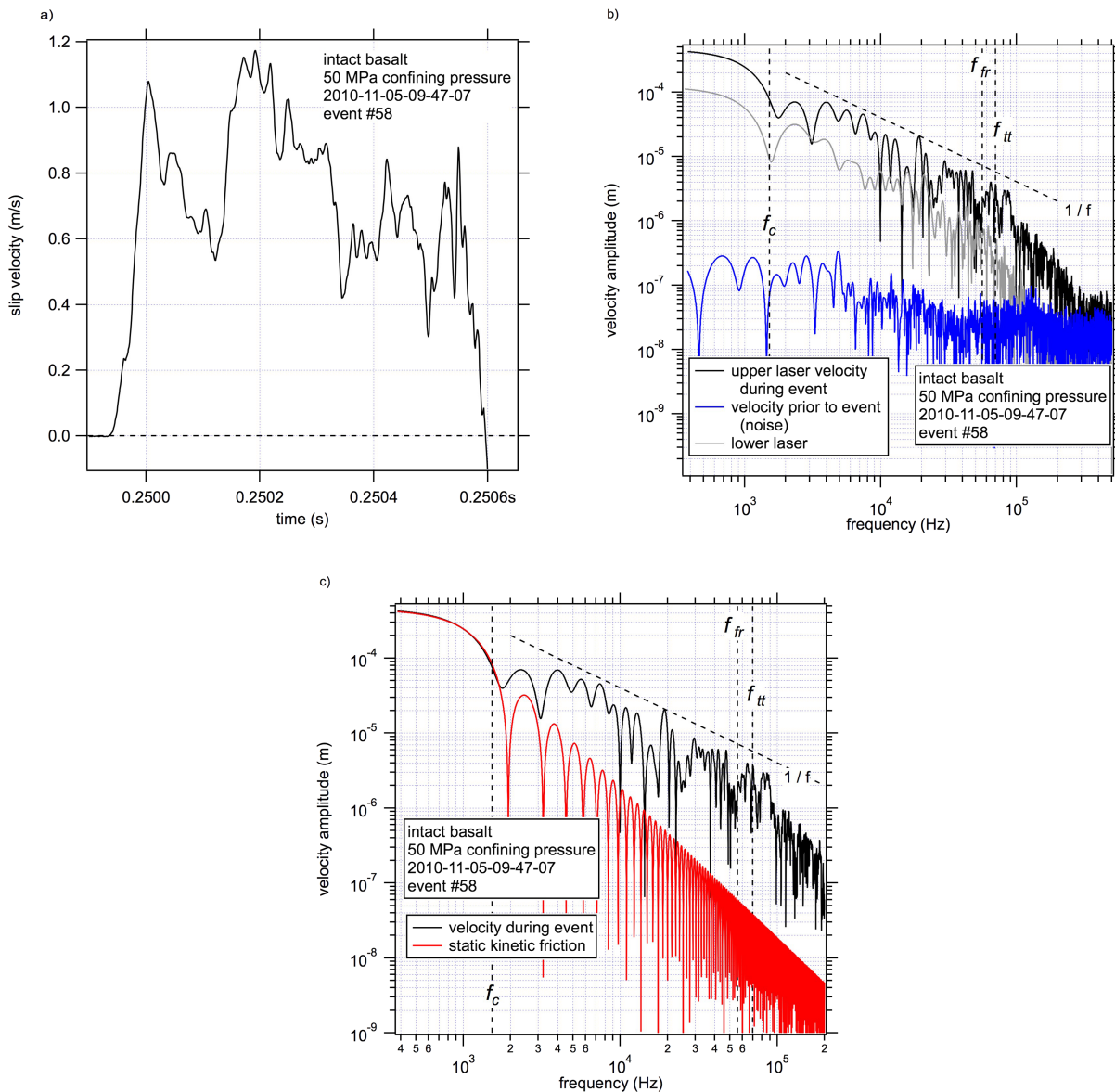
**Figure 6.** Velocity time series and amplitude spectra from failure of initially intact basalt at 50 MPa confining pressure. (a) Slip velocity time series. (b) Velocity amplitude spectrum with noise level (blue), lower laser spectrum (gray), and $1/f$ reference. (c and b) Velocity amplitude spectrum with noise level (blue), lower laser spectrum (gray), and $1/f$ reference. (c) Spectrum shown in part (b) with the velocity spectrum of a slider-block model following a static-kinetic fault strength (*Johnson and Scholz*, 1973) as a reference (red).

Appendix B provides details of all four of the fracture surface slip events, while the main text focuses on single representative granite and basalt events. During loading of the shear fracture surfaces of Westerly granite (Figure 7), two failure events occurred. Loading following the second event resulted in stable sliding. The slip velocity time series of the unstable events are both shorter duration and clearly less complex than rock failure, approximating a triangular shape. Consequently, the event corner frequency is at higher frequency $f_c = 3906$ Hz, as might be associated with a somewhat lower fracture energy. Above the corner, the spectral amplitude decay with frequency is much steeper than for rock failure, at nearly $1/f^2$. Empirically, this observation suggests that slip on rough surfaces may be depleted in high frequency content, relative to rock failure. This may be a misleading result, however, as is subsequently discussed. As before, the estimated rupture travel and reflection times are $f_{tt} = 7.46 \times 10^4$ Hz and $f_{fr} = 5.97 \times 10^4$ Hz, respectively, and are not associated with obvious resonances.
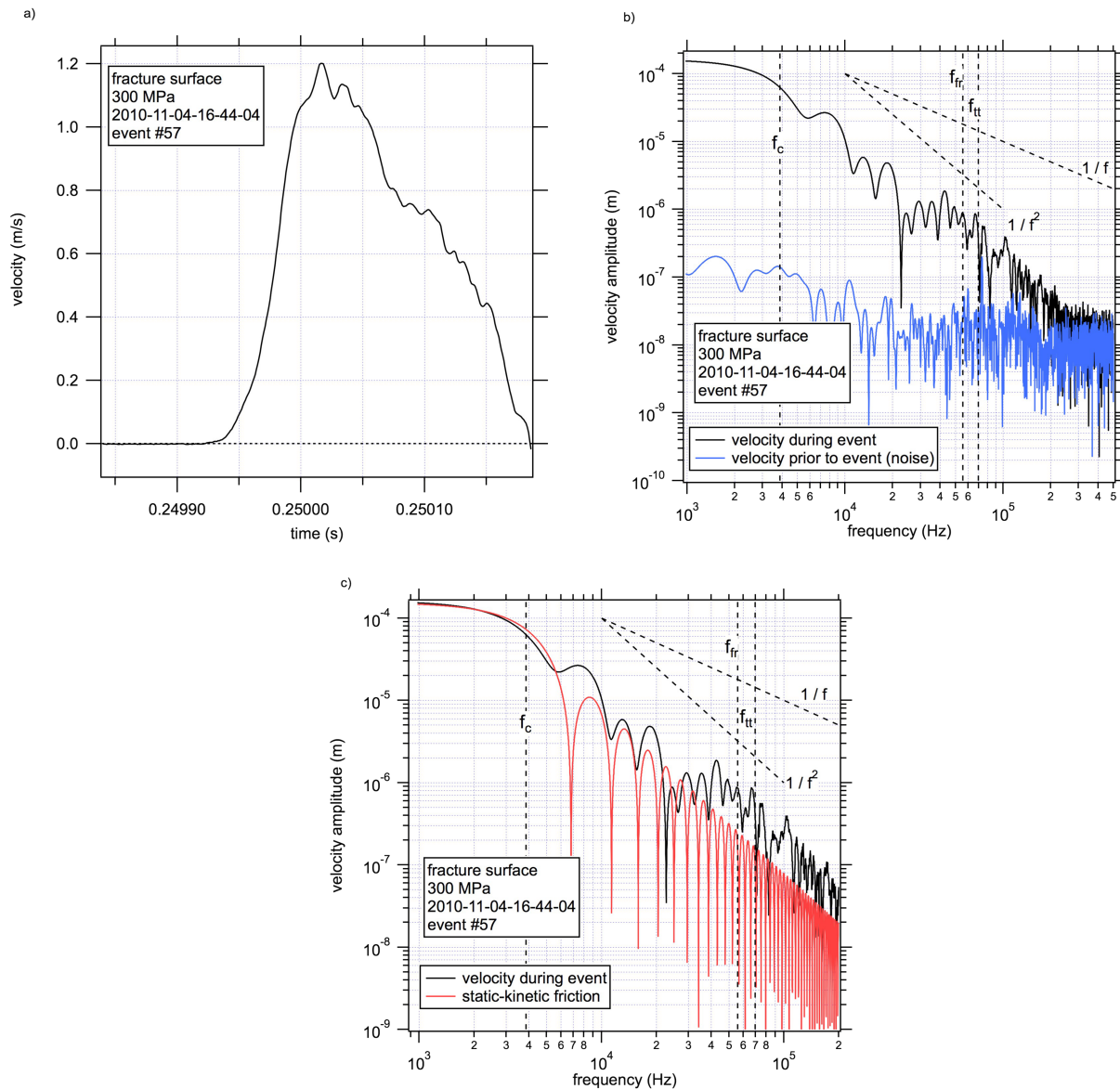
**Figure 7.** Granite slip event at 300 MPa confining pressure on a fractured surface that was generated during the failure event shown in Figure 5. (a) Velocity time series. (b) Velocity amplitude spectrum with noise level (blue) and $1/f$ reference. (c) Spectrum in (a) with the static-kinetic solution (red).

Similar results are found for slip on fracture surfaces of basalt (Figure 8). Again two failures were recorded. The experiment was stopped after the second failure. As for granite, the slip velocity time series is both shorter duration and less complex than for intact failure (Figure 8a). Above the corner, the decay with frequency is approximately $1/f^2$ (Figure 8b). Neither the estimated rupture travel nor reflection times of $f_{tt} = 7.46 \times 10^4$ Hz and $f_{fr} = 5.97 \times 10^4$ Hz, respectively, are associated with clear features in the spectra. A notable observation is an apparent postpeak oscillation in the time series (Figure 8a, question marks). This is manifest in the transform as a deviation from the reference between 10 and 20 kHz, labeled with a question mark in Figure 8c. The origin of this feature is unknown, but it has the appearance of a system resonance.

## 4. Discussion
### 4.1.1. Comparison With Natural Sources
As discussed previously in section 2.1, it is not straightforward to compare the experimental spectra (Figures 5–8) acquired in the near-field with natural far-field seismograms. Instead, we compare the experimental spectra with a plausible on-fault source spectrum of a natural earthquake, a Brune source model
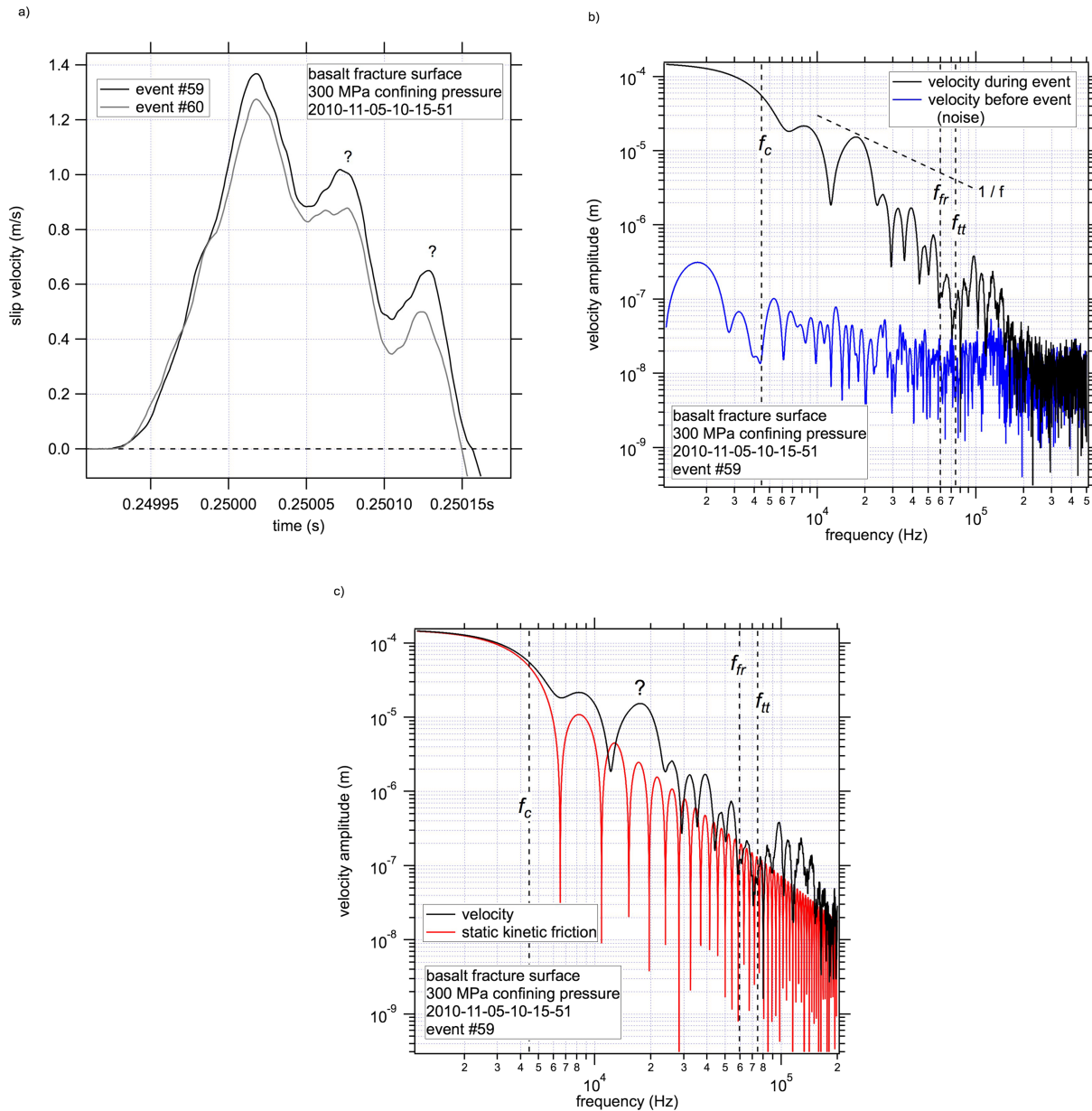
**Figure 8.** Basalt slip event at 300 MPa confining pressure on a fractured surface that was generated during the failure event shown in Figure 6. (a) Velocity time series. (b) Velocity amplitude spectrum with noise level (blue) and $1/f$ reference. (c) Spectrum in (a) with the static-kinetic solution (red).

(Brune, 1970). The Brune source has a far-field spectrum that is consistent with natural observations. Acknowledging that the particular time domain representation of a Brune source is unlikely to be relevant to stick-slip or rock fracture laboratory experiments, it is assumed that its frequency domain representation is that of a typical earthquake. While this is not ideal, application of specific source models in the frequency domain without regard for their implications in the time domain is done routinely in source seismology. The on-fault velocity amplitude spectrum of a Brune source is

$$A(\omega) = \frac{2\beta\Delta\tau}{\mu\sqrt{\left(\frac{1}{t_c}\right)^2 + \omega^2}}, \tag{4}$$

(see Appendix A1) where $\beta$ is the shear wave speed, $\mu$ is shear modulus, $\Delta\tau$ is the stress drop, and $t_c$ relates to the corner frequency as $1/f_c$, but is not equivalent to the event duration. In this case, the total slip is $\Delta\delta = 2\beta\Delta\tau t_c/\mu$.

At high frequency, the on-fault Brune velocity spectrum decays as $1/f$ consistent with the granite and basalt rock failure data at high frequencies. The overall spectral shape differs somewhat from the Brune model; this is shown in Figure 5c, where the Brune model is in green. The fracture experiments are somewhat depleted in high frequency energy relative to the Brune model; the falloff follows $\sim 1/f$ but is uniformly shifted to lower amplitudes. Current understanding of the spectrum of laboratory sources is limited, but it is known that the duration of these events is strongly influenced by the testing machine time constant (e.g., Kilgore et al., 2017; equation [(3)]). In contrast, for natural earthquakes (and conceptually the Brune model), duration is controlled by rupture propagation that is largely absent in our experiments. Accordingly, it is reasonable to suspect that the offset between our experimental spectra and that of a natural earthquake (and of the Brune model) is unavoidable. If that is correct, then rupture arrest and total moment in the experiments are decoupled from the on-fault rheology and fracture energy (see below); these are a topics of ongoing work.

The offset between a Brune velocity spectrum and the rock failure velocity spectrum notwithstanding the similarity in the spectral decay suggests that intact rock failure has high frequency complexity consistent with earthquakes. For the purpose of discussion, assume that the high frequency component can arise in experiments in two different ways: (1) intrinsically, where the event itself involves the creation of sources of high frequency or (2) from unsteady fault slip—acceleration and deceleration during rupture propagation, arrest, or other circumstances in which the slip is on a coherent fault surface but undergoes abrupt variations in rate. In the Earth, this second case would correspond to, for example, the interaction of the propagating rupture with strength and geometric heterogeneity, as in actual and conceptual models of ground motion complexity (Dunham et al., 2011; Andrews & Ma, 2016; *Lavellee et al.*, 2006). Our favored interpretation of the intact failure data is that the origin of the high frequency is largely intrinsic: that shear produces significant sources of high frequency energy, the creation of micro- and macroscopic brittle fractures (Goebel et al., 2014; Moore & Lockner, 1995). In other words, the fracture and brittle processes necessary to create a rough fault surface from initially intact rock and to displace it rapidly produce high frequency radiated energy from fracture creation over a wide range of scales.

### 4.1.2. Frequency Content of Fault Slip

Following from a qualitative comparison with the high frequency decay of the Brune model, it is clear that spectra from rough faulting experiments are depleted in high frequency energy relative to natural earthquakes of similar moment, decaying more closely as $1/f^2$ rather than $1/f$. This significant difference is unexpected. At present the exploratory nature of the work has not led to a definitive explanation. Two candidate considerations for future investigation come to mind. The first relates to radiation generated by unsteady slip within a coherent fault zone. To prevent high frequency radiation due to acceleration or deceleration, the fault must be fundamentally resistant to rapid changes in slip rate over a wide range of scales. So while rough surfaces are usually invoked to argue that small-scale rapid acceleration is possible at releasing portions of the surface geometry and rapid deceleration is possible at restraints, that may only be strictly correct for true discontinuities. Indeed, a fault surface with a power law amplitude distribution (Power & Tullis, 1991) is by definition a surface that has geometric barriers to resist slip at all wavelengths, as well as geometric encouragements. The experiments in this study are on rough surfaces, but which are mismatched and partially or completely separated by an intervening layer of rock flour and debris material. So there is a finite width shear zone of more compliant fault gouge that is coupled to the rough surfaces. The presence of gouge tends to damp rapid changes in slip rate and increase the weakening distance (Dieterich, 1981; Marone & Kilgore, 1993). It is also relatively well known that rougher surfaces generate more wear material (Okubo & Dieterich, 1984; Power et al., 1988). While in principle the rougher the surface, the more potential for roughness to have coseismic influence (Dunham et al., 2011; Fang & Dunham, 2013), in actuality rougher surfaces may be more decoupled from each other; the larger the roughness of the rock surfaces, the larger the role of the intervening shear zone. Given the well-documented presence of ultracataclasites in mature natural fault zones (Chester et al., 2004), a trial argument is that this material's existence is due to shear and that its mechanical purpose is to isolate subsequent shear within a weak layer remote from the stronger surroundings. An effect may also be to damp out the expected mechanical influence of roughness during fault slip. This idea is counter to the prevailing view in earthquake physics.

### 4.1.3. Machine Effects on Energy Release During Frictional Sliding

Another consideration is whether the resulting spectra are unduly influenced by experimental conditions. For instance, consider the most idealized model of a rapid, seismic laboratory slip event: a spring slider-

block model (Johnson & Scholz, 1976; Shimamoto et al., 1980). If you assume that the fault loses strength immediately at failure and slides under constant shear resistance, the spectrum of slip velocity decays as $1/f^2$ (see Appendix A). This spectral shape is very similar to the observations from the rough faulting experiments, as shown in Figures 7c and 8c (red). The comparison illustrates the potential for the finite mechanical system to impose a particular spectral shape. Unfortunately, conducting the rough surface frictional failure experiments at elevated confining stress of 300 MPa may coincide with conditions that artificially impose this spectral shape, as is argued next.

Immediately above and in the following section, the term "frictional" refers to faulting that depends on the absolute stress level, owing to a proportionality or linear relation between shear strength and normal stress (a friction coefficient $\mu$). Alternatively, this can be thought of as a 'pressure-dependent' fault strength because, for frictional faulting in a triaxial apparatus, the fault normal stress $\sigma_n$ is linear with confining pressure $\sigma_c$. For a fault that obeys the Coulomb failure criterion, the relationship is $\sigma_n = (\sigma_c + Ac)/(1 - A\mu)$, where $c$ is cohesion and $A$ is geometrical factor dictated by the angle between the fault and the axial piston $\beta$, $A = (1 - \cos2\beta)/\sin2\beta$. In this context, as a thought experiment, imagine that there is a high frequency component associated with dissipative processes in an experimental fault zone; perhaps the processes are the generation of fractures or on-fault roughness or rate dependences that produce unsteady slip. Regardless of the physical origin, so long as this high frequency component does not increase as fast with pressure as the energy available to be released increases, then the high frequency contribution can be made relatively small so as to be unimportant at high pressure.

Here, we use a general energy accounting that can accommodate the balance of radiated, latent, and dissipated energy either for natural earthquakes or for laboratory experiments (e.g., Savage & Wood, 1971; McGarr, 1994; Figure 9). In this diagram energy is normalized by fault area, to have units of J/m$^2$. In this example, it is assumed that the total coseismic energy is partitioned into heat from frictional sliding, "fracture energy," and radiated energy. The shear stress overshoots fault strength dynamically, as is thought to be typical of most earthquakes (e.g., McGarr, 1999) and for laboratory events (Lockner et al., 2017; Lockner & Okubo, 1983; McGarr, 1994). The stress overshoot is the difference between the static and dynamic stress drops.

In fracture mechanics-based earthquake source models, complexity of the faulting process, e.g., off-fault damage, damage induced by fault roughness, and on-fault rate dependences, are characterized as contributions either to the fracture energy term, the shear resistance above the residual coseismic strength (e.g., Wong, 1982, 1986), or to frictional sliding (Ida, 1972; Andrews, 1976; Ampuero & Rubin, 2008; Dunham et al., 2011). For simplicity, we use linear slip weakening (*Palmer and Rice*, 1972) to define the fracture energy, $G_e = \Delta\tau_d \, d_c/2$. Here, $\Delta\tau_d$ is the strength loss (dynamic stress drop), and $d_c$ is the weakening distance. The elastic unloading of the fault defines an energy that is available to be radiated, $E_a = \Delta\tau_s \Delta\delta/2$, where $\Delta\tau_s$ is the static stress drop and $\Delta\delta$ is the total slip. For seismic fault slip with this energy accounting (Figure 9a), the requirement is that the available energy exceeds all of the dissipative energies, $E_a > G_e + \Delta\tau_s(\Delta\tau_s - \Delta\tau_d)/k$, where the unloading stiffness $k = \Delta\tau_s/\Delta\delta$. The term $\Delta\tau_s(\Delta\tau_s - \Delta\tau_d)/k$ is energy partitioned in shear heating in excess of the final stress level (the dashed rectangle in Figure 9a).

Due to the dependence of shear resistance on normal stress, increasing the confining pressure decreases $G_e$ relative to $E_a$, as follows. The static and dynamic stress drops are pressure dependent, e.g., $\Delta\tau_s = \Delta\mu_s \, \sigma_e$ and $\Delta\tau_d = \Delta\mu_d \, \sigma_e$, where $\Delta\mu_s$ and $\Delta\mu_d$ are constants (e.g., Wong, 1986). Fracture energy therefore increases in proportion to normal stress (confining pressure) as $G_e = \Delta\mu_d \sigma_e d_c/2$. In contrast, the available energy and the shear heating term involve the product of stress drop and fault slip, both of which increase with confining stress. That is, the available energy can be equivalently expressed as $E_a = \Delta\tau_s^2/2\,k$. Because the available energy goes as normal stress squared, $E_a = (\Delta\mu_s \sigma_e)^2/2\,k$, it increases more rapidly with stress level than fracture energy. Similarly, the shear heating contribution is $\sigma_e^2(\Delta\mu_s - \Delta\mu_d)/k$.

A schematic example of how available energy, fracture energy, and the contribution from shear heating change with confining pressure is shown in Figure 10 for the case where the overshoot is fixed at 30% (the dynamic stress drop is 70% of the static stress drop). Fracture energy is plotted over the whole range of confining pressure (dashed), while the shear heating contribution (dash-dot) to the energy balance (Figure 9) is only defined at confining pressures where the available energy $E_a > E_d = G_e + \Delta\tau_s(\Delta\tau_s - \Delta\tau_d)/k$. At these
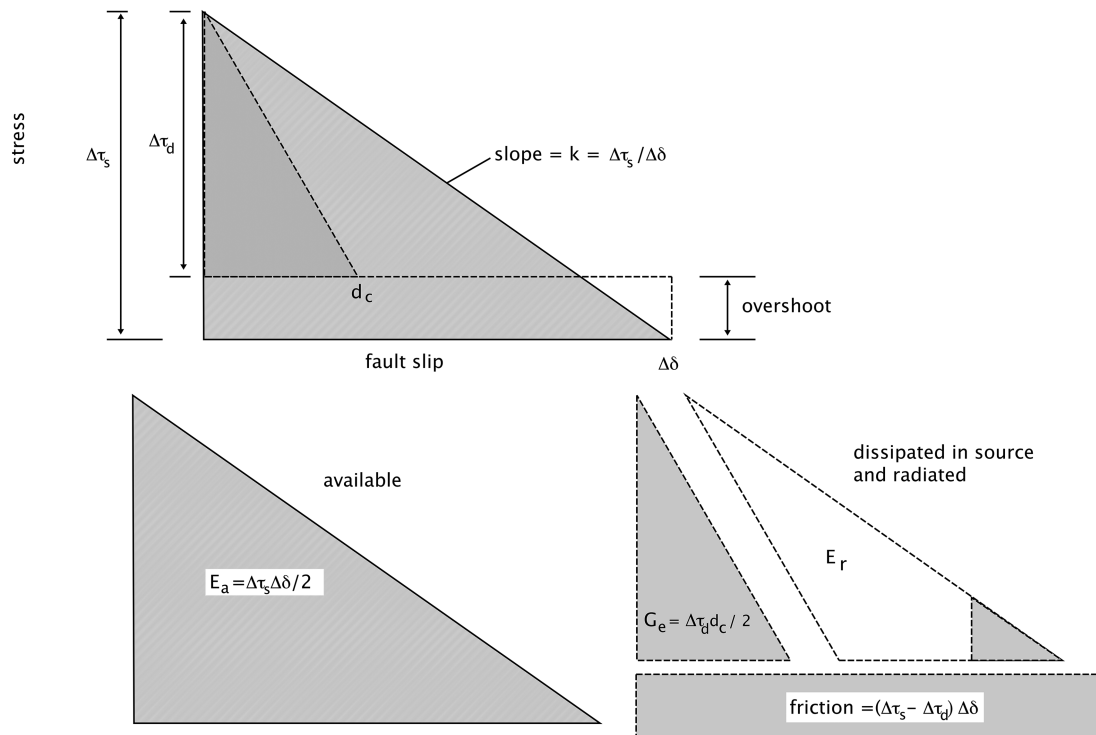
**Figure 9.** Energy balance with overshoot. Schematic stress-slip energy budget diagram of an earthquake or seismic laboratory slip event after *McGarr* [1994]. Top composite diagram shows the entire budget. Lower diagram breaks out the individual components of the balance: on the left is available energy, $E_a$, that is balanced between, on the right, fracture energy, $G_e$, radiated energy, $E_r$, and frictional heating in excess of the final stress. Strength loss here follows linear slip weakening (Ida, 1972; Palmer and Rice, 1973). The rate that stress is reduced in the surroundings with slip is the stiffness $k = \Delta\tau_s/\Delta\delta$, the ratio of the static stress drop to total slip. For the Earth, $k$ is the stiffness of the fault system. In a laboratory experiment, $k$ is the stiffness of the mechanical system that includes the fault, rock samples, and machine. The fracture energy $G_e = \Delta\tau d_c/2$ is the area defined by the strength loss (dark shaded region) and the residual strength level. In this example the shear stress overshoots the shear resistance by the difference between the dynamic and static stress drops, $\Delta\tau_s - \Delta\tau_d$. The available energy, the maximum possible radiated energy, is $E_a = \Delta\tau_s\,\Delta\delta/2$ (light shaded).

confining levels, stress drops produce radiated energy. Shown in red is the total dissipated energy, $E_d$, the sum of fracture energy and the shear heating contribution. The amount of radiated energy, $E_r = E_a - E_d$, grows with confining pressure. The implication is that in a laboratory experiment, high frequency energy release from frictional dissipative processes can be made arbitrarily small relative to the total released energy by increasing confining or normal stress. Our argument is that at excessive confining pressure, on-fault dissipation plays an insignificant role in the dynamic response of the mechanical system. The confining stress is extremely high in our rough faulting tests, and the observed spectra are consistent with a model laboratory event (slider-block spectrum) where on-fault processes do not contribute to the high frequency energy release. This energy release argument (Figures 9 and 10) is our favored explanation of the high frequency-deficient spectra from the rough fault experiments.

### 4.1.4. Near-Critical Energy Release of Earthquakes

The above argument implies that in a laboratory experiment to access earthquake-like source properties and spectra, the conditions (stress level) have to be set so the energy release does not greatly exceed the dissipation within the source. Accordingly, laboratory events in which the energy release is excessive relative to in-source dissipation, such as the rough faulting events at 300 MPa confining stress, are potentially "overdriven" and unnatural. Conversely, complexity in natural acceleration spectra may simply mean that the energy released as radiation is nearly balanced by dissipation in the source. Such events might be described as "near-critical." The idea of a close balance of radiated energy and in-fault zone dissipation implies that natural earthquake ruptures have significant barriers to continual expansion and are always on the verge of stopping.

The latter equivalently means that in-fault dissipation increases with propagation distance. Using our simple available energy release for an expanding rupture with stiffness $\mu/L$, the available energy increases as $L\Delta\tau_s^2/$
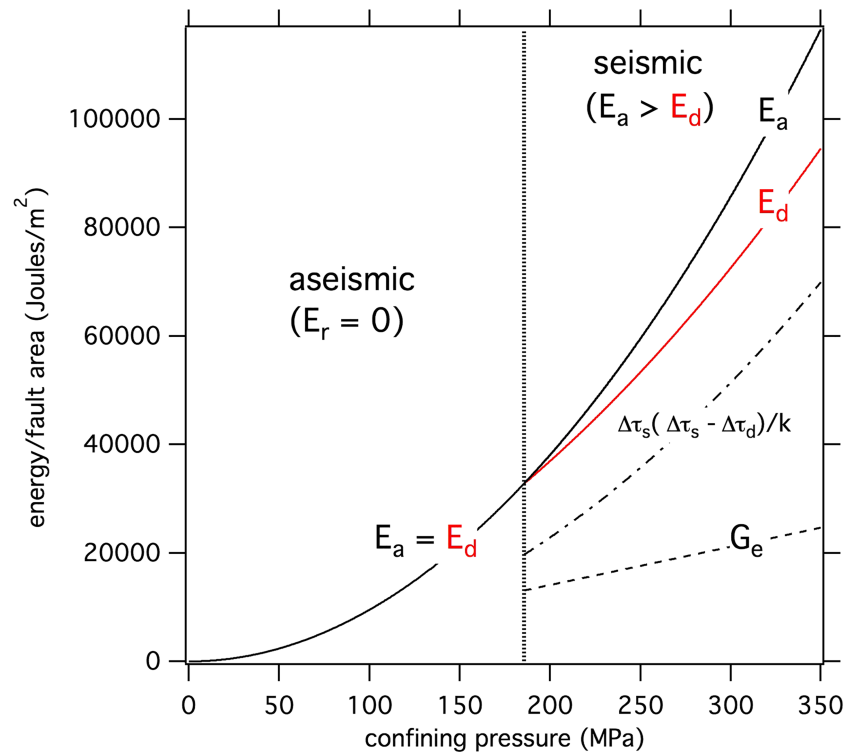
**Figure 10.** Variation of energy contributions with confining pressure in triaxial laboratory friction experiments. The energy balance/accounting is for overshoot, as in Figure 9. Shown are the fracture energy $G_e$, contributions from friction (dash-dot, labeled $\Delta\tau_s(\Delta\tau_s - \Delta\tau_d)/k$), the combined dissipative energy, $E_d = G_e + \Delta\tau_s(\Delta\tau_s - \Delta\tau_d)/k$, and the available energy $E_a$. The diagram is divided into the aseismic portion at low confining stress and seismic at high stress. At low confining stress, the strength loss is too small to generate radiated energy, $E_r$. At higher confining stress, the available energy exceeds that dissipated by faulting. The difference is the radiated energy. The stress drops are assumed to increase linearly with normal stress and the percent overshoot (30%) (Figure 9) is independent of normal stress. The values shown are calculated for cohesionless fault slip with friction coefficient, $\mu = 0.7$, linear slip weakening ($d_c = 400$ μm), $k = 0.133$ MPa/μm with a static stress drop of $0.3\sigma_e$ on a saw cut inclined at 30° from the piston axis.

2 $\mu$; for the rupture to remain near critical, then it requires that $G_e$ be also proportional to $L$. The fundamental idea that earthquakes show near-critical energy release has a very long history in the dynamic fracture mechanics and earthquake physics literature. Indeed, that "fracture energy" must increase with rupture size has been long known (Andrews, 1976; Ida, 1972). This idea can be accommodated with a linear slip weakening model, as in the original studies or in the context of more sophisticated, scale-dependent weakening relations (Abercrombie & Rice, 2005; Viesca & Garagash, 2015). Similar ideas are that the volume that undergoes near-source yielding increases with distance of propagation (Andrews, 1976) and that rupture propagation rates are fixed by scale-increasing in-source dissipation (Ida, 1973; Kostrov, 1966). A related idea is that natural earthquake stress drops reflect a near balance between energy released to the far-field and that dissipated in the source. In other words, the typically small, magnitude-independent earthquake stress drops (Hanks, 1977) are just a remotely observed, stress-parameterized measure of small net excess energy release.

## 5. Prior Studies of Failure Spectra: Slip On Flat Homogeneous Faults

Prior studies of the source spectra of laboratory faulting also should be considered in this context. The six prior studies, Schubnel et al. (2011), McLaskey et al. (2012), McLaskey and Lockner (2014), McLaskey, Kilgore, et al. (2015), Passelègue et al. (2016), and Marty et al. (2019), were conducted at significantly different conditions than our experiments. Schubnel et al. (2011) measured accelerations on flat smooth photo-elastic material (Columbia resin) at loads less than or equal to 9 kN, using 14 component arrays of piezo sensors (PZT–PI ceramic, PI255). The acceleration amplitude spectra are approximately frequency independent

out to nearly 40 kHz, consistent with the shape of natural earthquake spectra. McLaskey et al. (2012) studied recurring failure at different loading rates on flat, smooth, and rough surfaces of poly (methyl methacrylate) (PMMA, aka lucite, plexiglass, perspex) at very low normal stress (36 to 130 kPa). Frequency content was determined using the displacement amplitude spectra recorded by a single Panametrics V103 sensor. For the smooth surfaces, the spectral falloff of displacement amplitude was intermediate between $1/f^2$ (Brune- or earthquake-like) and $1/f$ (enriched in high frequency relative to natural earthquakes). For the rough surfaces, the spectral falloff of displacement amplitude varied from between $1/f^3$ (depleted in high frequencies relative to natural earthquakes, not unlike our very rough surfaces) up to approaching $1/f$ (enriched in high frequencies). Conceptually, similar results were found for flat, smooth (#600 grit) granite surfaces at 40, 80, and 120 MPa confining stress in triaxial geometry by McLaskey and Lockner (2014). Frequency content was determined using displacement recorded on a network of custom piezoelectric sensors and reported as moment spectra. The spectral falloff at all confining stresses is approximately $1/f^2$, consistent with a Brune model and natural earthquakes. Similar results were found for large (2 m long) unconfined, flat, smooth granite surfaces at low normal stress (5 MPa) using a network of Panametrics V103 sensors by McLaskey, Kilgore, et al. (2015). The moment spectra decay as $1/f^2$, again consistent with natural earthquakes. *Passeleque et al.* (2016) and Marty et al. (2019) used the same sensors as Schubnel et al. (2011) but on flat saw cut surfaces of Westerly granite, roughened with #160 (*Marty et al.*) or #240 grit (*Passelegue et al.*) grinding compound at between 10 and 90 MPa confining stress. The acceleration amplitude spectra are approximately frequency independent out to 100 kHz, consistent with natural earthquakes.

In summary, these prior studies show that slip on flat surfaces can produce enhanced high frequency contributions which vary with frequency in a way similar to natural earthquakes and our intact failure experiments. This is contrary to the prevailing view from earthquake physics source simulations (Dunham et al., 2011; Andrews & Ma, 2016), in which complex motion arises only in the presence of fault heterogeneity. Given the geometric differences between intact failure and slip on flat surfaces, it can only be concluded at this point that disparate source properties can lead to the same spectral decay. This may not be surprising considering that a Brune model, which looks nothing like an earthquake in the time domain, has earthquake-like spectra. It may also help to rationalize why the shape of natural earthquake spectra apparently does not depend strongly on magnitude or depth. However, none of these consolations are very satisfying. Satisfying would be a definitive physical explanation of how a slip on a flat smooth surface of plastic, particularly at 130 kPa normal stress (McLaskey et al., 2012), could ever produce significant earthquake-like, noise-like, complex high frequency radiation.

### 5.1. Complex Slip On Flat Faults

To develop a qualitative idea how complex slip on flat surfaces in prior studies arises, start by considering the most extreme case of the low stress analog experiments (McLaskey et al., 2012; Schubnel et al., 2011). Assume, reasonably, that there are no intrinsic sources of radiation (e.g., fracturing). Doing so leaves no alternative than to require rapid variations in fault slip rate to produce high frequency radiation. The fault having homogeneous frictional properties would further require that the unsteady slip rate results from interaction of the fault with changes in stress, for example, from coseismic reflections or free surface effects. Coseismic variation of slip rate arising from free surface effects is known to occur even at low normal stress in experiments on flat rock surfaces (Beeler et al., 2012; McLaskey, Kilgore, et al., 2015). Empirically, McLaskey et al. (2015) found that high frequency energy is strongly spatially and temporally correlated with rupture fronts that initiate when rupture intersects the fault ends. Reflections could also be important in all experimental geometries, and, while as yet these have not been quantified, their magnitude could be directly measured with strain gauges or estimated using known elastic contrasts.

For a stress perturbation to produce a variation in slip rate obviously requires the coseismic fault rheology to be stress sensitive. The frequency range of interest in the McLaskey, Kilgore, et al. (2015), Passelègue et al. (2016), Schubnel et al. (2011), and Marty et al. (2019) experiments is high, up to 100 kHz. The high frequency suggests a nearly instantaneous response to stress change. Instantaneous stress sensitivity is ubiquitous in low and high temperature rock deformation: friction (Dieterich, 1979), fracture (Scholz, 1968), and crack growth (Atkinson & Meredith, 1987a, 1987b), including well-characterized dynamic weakening mechanisms—flash weakening (Rice, 1999, 2006) and shear melting (Nielsen et al., 2008). In particular, in the brittle regime, friction, fracture, and crack growth have weak instantaneous logarithmic dependences of shear

stress (fault strength) on slip rate ($\tau \propto \ln V$). This means they have a strong and exponential dependence of slip rate on stress ($V \propto \exp\tau$). This fault rheology may lead naturally to highly unsteady slip rate in the presence of small stress perturbations. For brittle friction, the instantaneous dynamic stress changes are

$$\Delta\tau = a\sigma_e\ln\left(\frac{1}{X}\right), \tag{5}$$

as follows from Dieterich (1979) and Ruina (1983). Here, $\sigma_e$ is the effective normal stress, and $X$ is the ratio of slip velocities. As an example, evaluate equation (5) for a 10% change in slip speed ($X = 1.1$, e.g., a decrease in slip speed from 0.11 to 0.1 m/s) at conditions appropriate for the PMMA plastic experiments of McLaskey et al. (2012). Taking $a = 0.008$ and $\sigma_e = 36$ kPa, a tiny stress change of 0.03 kPa is required to produce the 10% change in slip speed. For a 100% change in slip speed ($X = 2$), the necessary stress change is still quite small, $\Delta\tau = 0.2$ kPa. Since the stress drops in the McLaskey, Kilgore, et al. (2015) study are on the order of 5.5 kPa, the above estimated stress changes would correspond to very weak reflections, about 0.5 % (0.03/5.5) and 4% (0.2/5.5) of the source excitation. While this idea to use the instantaneous rate dependence of friction to explain the observed complex spectra in prior studies has some appeal, it is speculation. That complex motion occurs on flat homogeneous faults at very low normal stress may also relate to our other speculative idea, expressed in the immediately preceding section. If complexity indicates near-critical behavior, the near-critical condition is most easily accessed in experiments at low normal stress.

Natural faults too invariably have nearby elastic contrasts, for example, among the relatively intact rock outside the fault zone, the ultracatclasite fault core and its surrounding damage zone (Chester et al., 1993; Chester et al., 2004; Chester & Chester, 1998; Chester & Logan, 1986). The structural architecture results from long-term near-fault inelastic strain partitioning. Seismologically, these contrasts may result in fault-zone waves (Ben-Zion, 1998; Ben-Zion & Aki, 1990; Li & Leary, 1990). Because of these geometric realities, near-fault reflections are a potential source of ground motion complexity (Ben-Zion, 1998). Depending on the degree of damage and confinement, modulus contrast across natural fault zones may differ from the contrast in our experiments. For instance, in the experiments, the difference between the shear modulus of confined granite (31.5 GPa, Martin et al., 1990) and steel (77 GPa) is on the order of 2x. For our study of experimental source spectra and for the Earth, more important than the details of the particular geometry and material properties is whether dynamic stress perturbations lead to complex motion of the fault itself. In other words, are there significant velocity changes during an earthquake as a result of self-generated stress transients? If so, the amplitude of dynamic stress perturbations and the resulting velocity changes could be used to constrain the dynamic fault rheology or at least to infer whether $V$ depends strongly on stress, or not.

## 6. Limitations of the Experiments

A few of the velocity spectra in this report contain machine resonances with periods less than the event duration, indicating that artifacts of the machine response influence the recorded motions. Fortunately, machine resonances that arise apparently routinely in double direct shear due to interactions between the two faults (see Kilgore et al., 2017) are not so obvious in the confined single fault triaxial faulting geometry used in the present study. An exception are the basalt slip events (Figure 7) that have a postpeak oscillation that may be due to resonance. An additional concern to be addressed in future studies is that more subtle interactions with the machine may be important in generating complex motion in triaxial experiments.

Experiments on rough fault surfaces at lower confining stress would have more direct relevance to the Earth than the tests at 300 MPa confining pressure conducted in the present study. Ideally experiments over a range of stress conditions would resolve whether enhanced high frequency radiation arises at near critical values of energy release. Establishing the range of stress and surface roughness conditions where laboratory failures are most directly analogous to natural earthquakes would be a valuable contribution.

A similar immediate shortcoming of all of these experiments is that the velocity measurements are made well off the fault, outside the pressure vessel. These are measurements of piston velocity, not fault slip. More ideally, fault slip would be measured directly. Within the vessel, rapid fault slip has not been reliably measured and will require specialized instrumentation development. Future experiments would benefit also from near-

fault stress measurements (Passelègue et al., 2016; Lockner et al., 2017) to determine relations among dynamic fault stress, acceleration, velocity, and slip.

## 7. Conclusions

In seismology, dynamic rupture modeling, and earthquake physics, high amplitude/high frequency motion has been attributed to complexity within the source, such as it arises from rapid slip in the presence of fault roughness or material heterogeneity. Near-fault velocity spectra of laboratory fault failures can have significant high frequency content. The failure of intact rock is the primary example of a laboratory source with strong high frequency radiation, having falloff of velocity amplitude with frequency of $1/f$ that resembles the spectra of natural earthquakes. As expected from models of rock fracture, the origin of this high frequency component during rock failure can be attributed to energy radiated from seismic fracture production over a wide range of scales below the total fault dimension. In contrast, subsequent slip events on the rough surfaces generated by rock failure are depleted in high frequency energy. The velocity amplitude spectra falloff approximately as $1/f^2$. The absence of a high frequency component may result from damping of the fault motion by the finite shear zone generated during the rock failure event or due to experimental procedures that minimize the contributions of on-fault shear resistance to the mechanics of failure. The latter is our favored explanation. Nonetheless, unsteady fault slip during laboratory failure on preexisting fault surfaces can produce high frequency radiation, with spectra consistent with earthquakes, for example, on flat, relatively smooth rock surfaces (McLaskey & Lockner, 2014; Passelègue et al., 2016) and on flat, smooth analog surfaces (McLaskey et al., 2012; Schubnel et al., 2011). Qualitative consideration of all the experiments to date suggests that the acceleration and deceleration of slip necessary to produce significant high frequency content (complex motion) that is consistent with earthquakes may arise when energy release is nearly balanced by on-fault dissipative processes. This near-critical energy release condition is most easily accessed at low normal stress in experiments.

## Appendix A: Reference Spectra

The standard technique of calculating the amplitude spectra from the Fourier transform of a time series, $f(t)$, is

$$F(\omega) = \int_{-\infty}^{\infty} f(t)\exp(-i\omega t)dt. \tag{A1a}$$

This results in a complex series in the frequency domain, $F(\omega)$. $\omega$ is the angular frequency, $\omega = 2\pi f$. From Euler's formula, equation (A1a) is equivalently

$$F(\omega) = \int_{-\infty}^{\infty} f(t)\cos(\omega t)dt - \int_{-\infty}^{\infty} f(t)i\sin(\omega t)dt. \tag{A1b}$$

The two integrals on the rhs of (A1b) are the real ($R(\omega)$) and imaginary parts ($I(\omega)$), respectively, of the complex frequency series. In seismology, the phase information contained in $F(\omega)$ is nearly always discarded, and only the magnitude of $F(\omega)$ as a function of frequency is used:

$$A(\omega) = \sqrt{R(\omega)^2 + I(\omega)^2}. \tag{A1c}$$

Throughout this report, equation (A1c) is referred to as the *amplitude* spectrum.

**Lab source.** The source spectra of laboratory events are influenced by the requirements of the mechanical system (sample and testing machine). In addition to determining the duration of the events largely independent of the properties of the fault (e.g., Johnson & Scholz, 1976), the mechanical system imposes constraints on the time history of velocity. Thus, it is possible for the shape of the amplitude spectrum to be dictated by the machine rather than by the fault. For example, the mechanical interactions between the testing machine and a fault can be extremely well characterized by an inertia-limited slider-block model (Johnson & Scholz, 1976; Shimamoto et al., 1980). Using this model, if the fault follows a static-kinetic friction relation where the
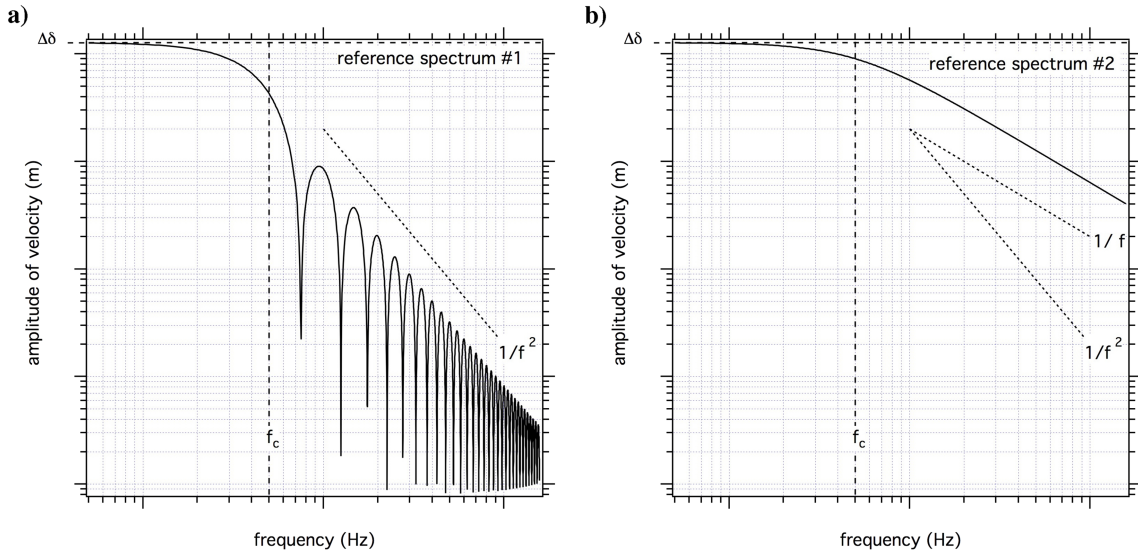
**Figure A1.** Reference velocity spectra. (a) On-fault velocity amplitude spectrum for an inertia-limited slider block that obeys a static-kinetic friction relation. The low frequency amplitude is the total displacement of the event, $\Delta\delta$, and the corner frequency is the reciprocal of event duration, $T/2$. Dotted reference line has slope $1/f^2$. (b) On-fault velocity amplitude spectrum of a Brune source. The low frequency amplitude is the total displacement of the event, $\Delta\delta$, and the corner frequency is the reciprocal of the characteristic time, $t_c$. Upper dotted reference line has slope $1/f$.

fault has zero slip rate until the stress reaches a failure stress $\tau_f$, and then fault strength immediately drops to a constant sliding strength $\tau_k$, the velocity time series during the event is

$$V = V_{peak}\sin\left(\frac{2\pi t}{T}\right) \quad 0 \le t \le \frac{T}{2}, \tag{A2a}$$

(Johnson & Scholz, 1976; Rice & Tse, 1986). Here the duration of the slip event, $T/2$, is half the resonance period of the machine, $T$. Duration is inversely proportional to the square root of the system stiffness, $k$, $T = 2\pi\sqrt{m/(Ak)}$, where $m$ is mass and $A$ is fault area. $V_{peak}$ is the peak velocity, determined by the machine properties and the dynamic strength loss: $\Delta\tau_d = \tau_s - \tau_k$, (the dynamic stress drop), such that $V_{peak} = 2\pi\Delta\tau_d/kT$.

The spectrum of (A2a) is given by

$$
\begin{aligned}
\frac{R(\omega)}{V_{peak}} &= \frac{1-\cos\left(\pi + \frac{\omega T}{2}\right)}{2\left(\frac{2\pi}{T} + \omega\right)} + \frac{1-\cos\left(\pi - \frac{\omega T}{2}\right)}{2\left(\frac{2\pi}{T} - \omega\right)}, \\[2em]
\frac{I(\omega)}{V_{peak}} &= \frac{\sin\left(\pi - \frac{\omega T}{2}\right)}{2\left(\frac{2\pi}{T} - \omega\right)} - \frac{\sin\left(\pi + \frac{\omega T}{2}\right)}{2\left(\frac{2\pi}{T} + \omega\right)}.
\end{aligned}
\tag{A2b}
$$

and equation (A1c). The amplitude spectrum (Figure A1a) is flat at low frequency with (DC) amplitude equal to the total displacement $\Delta\delta = 2\Delta\tau_d/k$. Thus, the DC amplitude is uniquely determined by machine properties and the static-kinetic strength loss. The transition from the DC amplitude to the constant rate of decay of log amplitude with log frequency is the corner frequency $f_c = 2/T$. For this model, duration is independent of the fault frictional properties. At high frequency, the amplitude decays as $1/f^2$.

**Brune source.** The on-fault particle velocity of a Brune source is

$$\dot{u} = \frac{\beta\Delta\tau}{\mu}\exp\frac{-t}{t_c}, \tag{A3a}$$

(Brune, 1970). Here, $\beta$ is shear wave speed, $\mu$ is shear modulus, $\Delta\tau$ is the on-fault dynamic stress drop, and $t_c$ is the time constant of the failure event. Equivalently, the velocity across the fault $V$ is twice the particle velocity:

$$V = \frac{2\beta\Delta\tau}{\mu}\exp\frac{-t}{t_c}. \tag{A3b}$$

To simplify in the following, the peak velocity is defined as $V_{peak} = 2\beta\Delta\tau/\mu$. The Fourier transform of equation (A3b) is

$$F(\omega) = V_{peak}\int_0^\infty \exp\frac{-t}{t_c}\cos(\omega t)dt + V_{peak}\int_0^\infty \exp\frac{-t}{t_c}i\sin(\omega t)dt, \tag{A4}$$

where the event is taken to start at $t = 0$ and the velocity to be zero at all times prior to the start. Carrying out the integration in (A4) results

$$R(\omega) = V_{peak}\left[\frac{\exp\frac{-t}{t_c}}{\left(1/t_c\right)^2 + (\omega)^2}\left(-\frac{1}{t_c}\cos\omega t + \omega\sin\omega t\right)\right]_0^\infty, \tag{A5a}$$

$$I(\omega) = V_{peak}\left[\frac{i\exp\frac{-t}{t_c}}{\left(1/t_c\right)^2 + (\omega)^2}\left(-\frac{1}{t_c}\sin\omega t - \omega\cos\omega t\right)\right]_0^\infty. \tag{A5b}$$

The two integrals in (A4) representing the real ($R$) and imaginary ($I$) parts have been separated. These evaluate to

$$R(\omega) = V_{peak}\left[\frac{-1}{\left(1/t_c\right)^2 + (\omega)^2}\left(\frac{1}{t_c}\right)\right], \tag{A6a}$$

$$I(\omega) = V_{peak}\left[\frac{-i}{\left(1/t_c\right)^2 + (\omega)^2}(\omega)\right]. \tag{A6b}$$

The velocity amplitude spectra of (A5) is

$$A(\omega) = \frac{V_{peak}}{\sqrt{\left(\frac{1}{tc}\right)^2 + \omega^2}} \tag{A7}$$

(Figure A1b).

### Slip On Rough fault surfaces

There are two slip events on each of the granite and basalt fracture surfaces. Representative events are shown in the main text of the paper. Here, the similarity of the paired events is presented in more detail. The velocity time series of the two granite slip events is shown in Figure B1a. In both cases, the onset is gradual, whereas arrest is more abrupt. The shape is asymmetric with the peak occurring early in the event. Unlike the slider-block solution (A2b), duration here is not constant, fixed by mass, area, and stiffness. Instead duration increases with event size (total slip), suggesting that duration scales with event moment (fault area is constant). This reflects the influence of dynamic fault properties that is missing from the slider-block model. Nevertheless, beyond the difference in duration and total slip (Figure B1b) that are manifest in the spectra as differences in DC level and corner frequency, the spectra are similar and generally consistent with the $1/f$ decay of amplitude predicted by the slider-block model.

The basalt slip events are more similar to each other (Figure B2a), though still not identical. They share the same gradual onset, more abrupt arrest than onset, and the general asymmetric shape as the granite slip events. They also show the same sense of duration-size (total slip) scaling. There is a strong similarity in specific shape, having two local maximums, postpeak. As noted in the text, these have the appearance
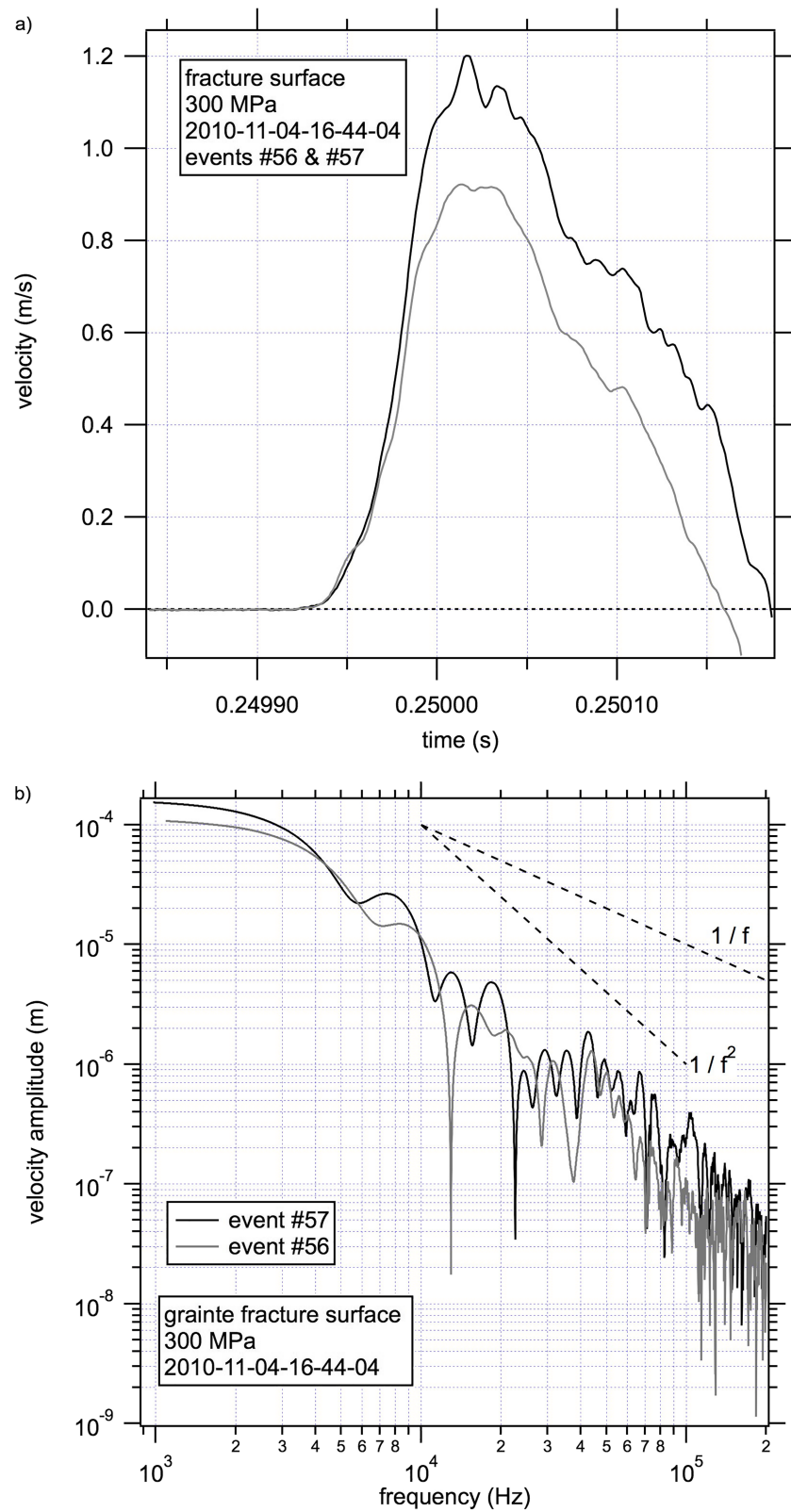
**Figure B1.** Granite fracture surface slip events. (a) Slip velocity time series. (b) Velocity amplitude spectra.
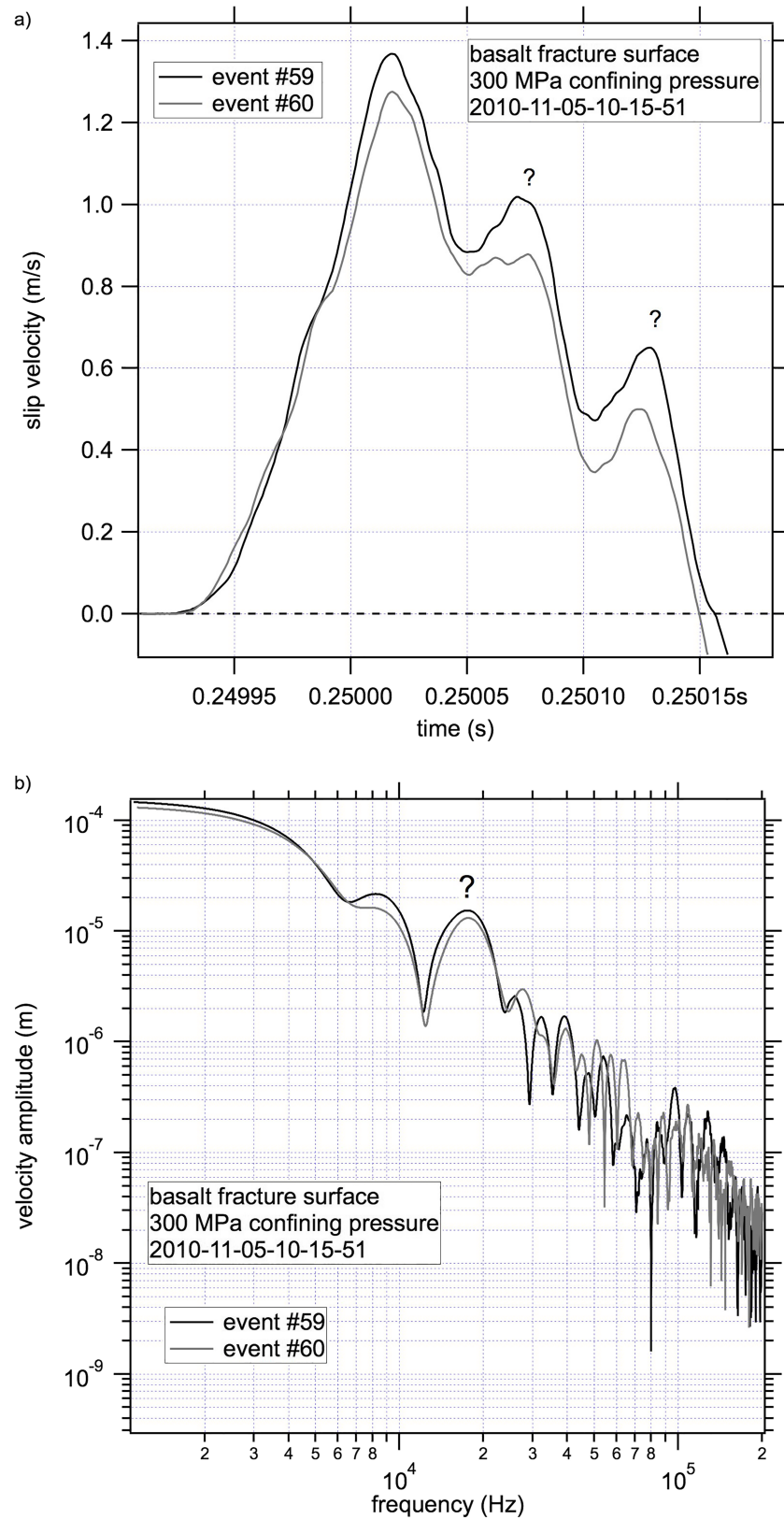
**Figure B2.** Slip on basalt fracture surfaces. (a) Slip velocity time series. (b) Velocity amplitude spectra. The question marks denote possible resonance within the sample assembly.

of a resonance. This feature is clear in the frequency domain (Figure B2b). It is intermediate between the corner and the reflection return times that define the elastodynamic frequencies. Most likely this arises from a resonance associated with the rock samples themselves or another small-scale component of the loading system. Though resonances are an unintended artifact of machine design, they may have some analogy to natural fault zone waves. The absence of this effect for granite may indicate differences in the fault response to coseismic stress changes.

# References

Abercrombie, R. E., & Rice, J. R. (2005). Can observations of earthquake scaling constrain slip weakening? *Geophysical Journal International*, *162*, 406–424.

Ampuero, J. P., & Rubin, A. M. (2008). Earthquake nucleation on rate and state faults: aging and slip laws. *Journal of Geophysical Research*, *113*(B01), 302.

Andrews, D. J. (1976). Rupture propagation with finite stress in anti-plane strain. *Journal of Geophysical Research*, *18*, 3575–3582.

Andrews, D. J. (1981). A stochastic fault model 2. Time-dependent case. *Journal of Geophysical Research*, *86*, 10,821–10,834.

Andrews, D. J., & Ma, S. (2016). Validating a dynamic earthquake model to produce realistic ground motion. *Bulletin of the Seismological Society of America*, *106*, 665–672.

Atkinson, B. K., & Meredith, P. G. (1987a). The theory of subcritical crack growth with applications to minerals and rocks. In B. K. Atkinson (Ed.), *Fracture Mechanics of Rock, Geol. Ser* (pp. 111–166). New York: Elsevier.

Atkinson, B. K., & Meredith, P. G. (1987b). Experimental fracture mechanics data for rocks and minerals. In B. K. Atkinson (Ed.), *Fracture Mechanics of Rock, Geol. Ser* (pp. 477–525). New York: Elsevier.

Beeler, N. M., Kilgore, B., McGarr, A., Fletcher, J., Evans, J., & Baker, S. R. (2012). Observed source parameters for dynamic rupture with non-uniform initial stress and relatively high fracture energy. *Journal of Structural Geology, Special Volume in honor of Toshi Shimamoto, Journal of Structural Geology, Volume*, *38*, 77–89.

Ben-Zion, Y. (1998). Properties of seismic fault zone waves and their utility for imaging low-velocity structures. *Journal of Geophysical Research*, *103*, 12,567–12,585.

Ben-Zion, Y., & Aki, K. (1990). Seismic radiation from a SH line source in a laterally heterogeneous planar fault zone. *Bulletin of the Seismological Society of America*, *80*, 971–994.

Brace, W. F. (1964). Brittle fracture of rocks. In W. R. Judd (Ed.), *State of stress in the Earth's crust* (pp. 110–178). New York, New York: Elsevier.

Brune, J. N. (1970). Tectonic stress and the spectra of seismic shear waves from earthquakes. *Journal of Geophysical Research*, *75*, 4997–5009.

Chester, F. M., & Chester, J. S. (1998). Ultracataclasite structure and friction processes of the San Andreas fault. *Tectonophysics*, *295*, 199–221.

Chester, F. M., Chester, J. S., Kirschner, D. L., Schultz, S. E., & Evans, J. P. (2004). Structure of large-displacement, strike-slip fault zones in the brittle continental crust. In G. D. Karner, B. Taylor, N. W. Driscoll, & D. L. Kohlstedt (Eds.), *Rheology and Deformation in the Lithosphere at Continental Margins* (Chap. 8, Vol. 2004, pp. 223–260). New York: Columbia University Press.

Chester, F. M., Evans, J. P., & Biegel, R. L. (1993). Internal structure and weakening mechanisms of the San Andreas fault. *Journal of Geophysical Research*, *98*, 771–786.

Chester, F. M., & Logan, J. M. (1986). Implications for mechanical properties of brittle faults from observations of the Punchbowl fault zone, California. *Pure and Applied Geophysics*, *124*, 79–106.

Cotton, F., & Coutant, O. (1997). Dynamic stress variations due to shear faults in a plane-layered medium. *Geophysical Journal International*, *128*, 676–688.

Dieterich, J. H. (1979). Modeling of rock friction: 1. Experimental results and constitutive equations. *Journal of Geophysical Research*, *84*, 2161–2168.

Dieterich, J. H. (1981). Constitutive properties of faults with simulated gouge. In N. L. Carter, & a. (Eds.), *Mechanical Behavior of Crustal Rocks*, Geophys. Monogr. Ser. (Vol. 24, pp. 103–120). Washington, D.C.: AGU.

Dunham, E. M., Belanger, D., Cong, L., & Kozdon, J. E. (2011). Earthquake ruptures with strongly rate-weakening friction and off-fault plasticity, Part 2: nonplanar faults. *Bulletin of the Seismological Society of America*, *101*, 2308–2322.

Fang, Z., & Dunham, E. (2013). Additional shear resistance from fault roughness and stress levels on geometrically complex faults. *Journal of Geophysical Research: Solid Earth*, *118*, 1–13. https://doi.org/10.1002/jgrb.50262

Goebel, T. H. W., Becker, T. W., Sammis, C. G., Dresen, G., & Schorlemmer, D. (2014). Off-fault damage and acoustic emission distributions during the evolution of structurally-complex faults over series of stick-slip events. *Geophysical Journal International*, *197*(3), 1705–1718. https://doi.org/10.1093/gji/ggu074

Hanks, T. C. (1977). Earthquake stress drops, ambient tectonic stresses and stresses that drive plate motion. *Pure and Applied Geophysics*, *115*, 441–458.

Hanks, T. C., & McGuire, R. K. (1981). The character of high-frequency ground motion. *Bull. Seism. Soc. Am.*, *71*, 2071–2095.

Hanks, T. C., & Wyss, M. (1972). The use of body-wave spectra in the determination of seismic-source parameters. *Bulletin of the Seismological Society of America*, *62*, 561–589.

Housner, G. W. (1947). Characteristics of strong-motion earthquakes. *Bull. Seism. Soc. Am.*, *37*, 19–31.

Ida, Y. (1972). Cohesive force across the tip of a longitudinal shear crack and Griffith's specific surface energy. *Journal of Geophysical Research*, *77*, 3796–3805.

Ida, Y. (1973). Stress concentration and unsteady propagation of longitudinal shear cracks. *Journal of Geophysical Research*, *78*, 3418–3429.

Johnson, T., & Scholz, C. (1976). Dynamic properties of stick-slip friction of rock. *Journal of Geophysical Research*, *81*, 881–888. 1976

Kilgore, B. D., McGarr, A., Beeler, N. M., & Lockner, D. A. (2017). Earthquake Source Properties From Instrumented Laboratory Stick-Slip. In M. Y. Thomas, T. M. Mitchell, & H. S. Bhat (Eds.), *Fault Zone Dynamic Processes: Evolution of Fault Properties During Seismic Rupture*. Hoboken, NJ, USA: John Wiley & Sons, Inc. https://doi.org/10.1002/9781119156895.ch8

Kostrov, B. V. (1966). Unsteady propagation of longitudinal shear cracks. *Journal of Applied Mathematics and Mechanics*, *30*, 1241–1248.

Lavallee, D., Liu, P., & Archuleta, R. J. (2006). Stochastic model of heterogeneity in earthquake slip spatial distributions. *Geophysical Journal International*, *165*, 623–640.

Li, Y.-G., & Leary, P. C. (1990). Fault zone trapped seismic waves. *Bulletin of the Seismological Society of America*, *80*, 1245–1271.

Lockner, D. A., Byerlee, J. D., Kuksenko, V., Ponomarev, A., & Sidorin, A. (1991). Quasi-static fault growth and shear fracture energy in granite. *Nature*, *350*, 39–42.

Lockner, D. A., Kilgore, B. D., Beeler, N. M., & Moore, D. E. (2017). The Transition From Frictional Sliding to Shear Melting in Laboratory Stick-Slip Experiments. In M. Y. Thomas, T. M. Mitchell, & H. S. Bhat (Eds.), *Fault Zone Dynamic Processes: Evolution of Fault Properties During Seismic Rupture*. Hoboken, NJ, USA: John Wiley & Sons, Inc. https://doi.org/10.1002/9781119156895.ch6

Lockner, D.A., D. Moore, N.M. Beeler and B.D. Kilgore, (2010), Surface Melt Produced on Faults During Laboratory Stick-slip Experiments, Abstract T23A-2245 presented at 2010 Fall Meeting, AGU, San Francisco, Calif., 13-17 Dec.

Lockner, D. A., & Okubo, P. G. (1983). Measurements of frictional heating in granite. *Journal of Geophysical Research*, *88*, 4313–4320.

Ma, K.-F., Brodsky, E. E., Mori, J., Ji, C., Song, T.-R. A., & Kanamori, H. (2003). Evidence for fault lubrication during the 1999 Chi-Chi Taiwan earthquake (Mw7.6). *Geophysical Research Letters*, 1244 *30*(7422). https://doi.org/10.1029/2002GL015380

Marone, C., & Kilgore, B. (1993). Scaling of the critical slip distance for seismic faulting with shear s train in fault zones. *Nature*, *362*, 618–621.

Martin R. J. III, Coyner, K. B., & Haupf, R. W. (1990). Physical properties measurements on analog granites related to the joint verification experiment, New England Research Report, GL-TR-90-0120 ADA230571. https://apps.dtic.mil/dtic/tr/fulltext/u2/a230571.pdf

Marty, S., Passelègue, F. X., Aubry, J., Bhat, H. S., Schubnel, A., & Madariaga, R. (2019). Origin of high-frequency radiation during laboratory earthquakes. *Geophysical Research Letters*, *46*, 3755–3763. https://doi.org/10.1029/2018GL080519

McGarr, A. (1994). Some comparisons between mining-induced and laboratory earthquakes, *Pure Appl. Geophysics*, *142*, 467–489.

McGarr, A. (1999). On relating apparent stress to the stress causing earthquake fault slip. *Journal of Geophysical Research*, *104*, 3003–3011.

McLaskey, G. C., Kilgore, B. D., & Beeler, N. M. (2015). Slip-pulse rupture behavior on a 2 m granite fault. *Geophysical Research Letters*, *42*, 7039–7045. https://doi.org/10.1002/2015GL065207

McLaskey, G. C., & Lockner, D. A. (2014). Preslip and cascade processes initiating laboratory stick slip. *Journal of Geophysical Research: - Solid Earth*, *119*. https://doi.org/10.1002/2014JB011220

McLaskey, G. C., Lockner, D. A., Kilgore, B. D., & Beeler, N. M. (2015). A Robust Calibration Technique for Acoustic Emission Systems Based on Momentum Transfer from a Ball Drop. *Bulletin of the Seismological Society of America*, *105*, 257–271. https://doi.org/10.1785/0120140170

McLaskey, G. C., Thomas, A. M., Glaser, S. D., & Nadeau, R. M. (2012). Fault healing promotes high-frequency earthquakes in laboratory experiments and on natural faults. *Nature*, *491*(7422), 101–104. https://doi.org/10.1038/nature11512

Moore, D. E., & Lockner, D. A. (1995). The role of microcracking in shear-fracture propagation in granite. *Journal of Structural Geology*, *17*, 95–114.

Nielsen, S., Di Toro, G., Hirose, T., & Shimamoto, T. (2008). Frictional melt and seismic slip. *Journal of Geophysical Research*, *113*, B01308.

Okubo, P. G., & Dieterich, J. H. (1984). Effects of physical fault properties on frictional instabilities produced on simulated faults. *Journal of Geophysical Research*, *88*, 887–890.

Passelègue, F. X., Schubnel, A., Nielsen, S., Bhat, H. S., Deldicque, D., & Madariaga, R. (2016). Dynamic rupture processes inferred from laboratory microearthquakes. *Journal of Geophysical Research: - Solid Earth*, *121*, 4343–4365. https://doi.org/10.1002/2015JB012694

Power, W., Tullis, T., & Weeks, J. (1988). Roughness and wear during brittle faulting. *Journal of Geophysical Research*, *93*(B12), 15,268–15,278. https://doi.org/10.1029/JB093iB12p15268

Power, W. L., & Tullis, T. E. (1991). Euclidean and fractal models for the description of rock surface roughness. *Journal of Geophysical Research*, *96*(B1), 415–424. https://doi.org/10.1029/90JB02107

Palmer, A. C., & Rice, J. R. (1973). The growth of slip surfaces in the progressive failure of over-consolidated clay. *Proc. R. Soc. London, Ser. A*, *332*, 527–548.

Rice, J. R. (1999). Flash heating at asperity contacts and rate-dependent friction, *EOS Trans. Am. Geophys. Un.*, *80*, F681.

Rice, J. R. (2006). Heating and weakening of faults during earthquake slip. *Journal of Geophysical Research*, *111*, B05311. https://doi.org/10.1029/2005JB004006

Rice, J. R., & Tse, S. T. (1986). Dynamic motion of a single degree of freedom system following a rate and state dependent friction law. *Journal of Geophysical Research*, *91*, 521–530.

Ruina, A. L. (1983). Slip instability and state variable friction laws. *Journal of Geophysical Research*, *88*, 10,359–10,370.

Savage, J. C., & Wood, M. D. (1971). The relation between apparent stress and stress drop. *Bulletin of the Seismological Society of America*, *61*, 1381–1388.

Scholz, C. (1968). Microfractures, aftershocks and seismicity. *Bulletin of the Seismological Society of America*, *58*, 117–130.

Schubnel, A., Nielsen, S., Taddeucci, J., Vinciguerra, S., & Rao, S. (2011). Photo-acoustic study of subshear and supershear ruptures in the laboratory. *Earth and Planetary Science Letters*, *308*(3–4), 424–432. https://doi.org/10.1016/j.epsl.2011.06.013

Shimamoto, T., Handin, J., & Logan, J. M. (1980). Specimen-apparatus interaction during stick-slip in a triaxial compression machine: a decoupled two-degree of freedom model. *Tectonophysics*, *67*, 175–205.

Simmons, G. (1964). Velocity of shear waves in rocks to 10 kilobars, 1. *Journal of Geophysical Research*, *69*, 1123–1130.

Tse, S. T., & Rice, J. R. (1986). Crustal earthquake instability in relation to the depth variation of frictional slip properties. *Journal of Geophysical Research*, *91*, 9452–9472.

Viesca, R. C., & Garagash, D. I. (2015). Ubiquitous weakening of faults due to thermal pressurization. *Nature Geoscience*, *8*, 875–879.

Wong, T.-f. (1982). Shear fracture energy of Westerly granite from post-failure behavior. *Journal of Geophysical Research*, *87*, 990–1000.

Wong, T.-f. (1986). *On the normal stress dependence of the shear fracture energy, in Earthquake Source Mechanics, Geophys. Monogr. Ser., Vol. 37, edited by S. Das et al., pp. 1-11*. Washington, D.C.: AGU.